University of South Florida

DIGITAL COMMONS
@ UNIVERSITY OF SOUTH FLORIDA

Digital Commons @ University of South Florida

School of Geosciences Faculty and Staff Publications

School of Geosciences

1-2021

Magma Source Evolution Following Subduction Initiation: Evidence From the Element Concentrations, Stable Isotope Ratios, and Water Contents of Volcanic Glasses From the Bonin Forearc (IODP Expedition 352)

Daniel A. Coulthard
Massey University

Mark K. Reagan
University of Iowa

Kenji Shimizu
Kochi Institute for Core Sample Research

Ilya N. Bindeman
University of Oregon

Maryjo Brounce
University of California Riverside

Follow this and additional works at: https://digitalcommons.usf.edu/geo_facpub

 Part of the Earth Sciences Commons

See next page for additional authors

Scholar Commons Citation

Coulthard, Daniel A.; Reagan, Mark K.; Shimizu, Kenji; Bindeman, Ilya N.; Brounce, Maryjo; Almeev, Renat R.; Ryan, Jeffrey; Chapman, Timothy; Shervais, John; and Pearce, Julian A., "Magma Source Evolution Following Subduction Initiation: Evidence From the Element Concentrations, Stable Isotope Ratios, and Water Contents of Volcanic Glasses From the Bonin Forearc (IODP Expedition 352)" (2021). *School of Geosciences Faculty and Staff Publications*. 2309.
https://digitalcommons.usf.edu/geo_facpub/2309

This Article is brought to you for free and open access by the School of Geosciences at Digital Commons @ University of South Florida. It has been accepted for inclusion in School of Geosciences Faculty and Staff Publications by an authorized administrator of Digital Commons @ University of South Florida. For more information, please contact digitalcommons@usf.edu.

Authors

Daniel A. Coulthard, Mark K. Reagan, Kenji Shimizu, Ilya N. Bindeman, Maryjo Brounce, Renat R. Almeev, Jeffrey Ryan, Timothy Chapman, John Shervais, and Julian A. Pearce

This article is available at Digital Commons @ University of South Florida: https://digitalcommons.usf.edu/geo_facpub/2309

Check for updates

Geochemistry, Geophysics, Geosystems

RESEARCH ARTICLE
10.1029/2020GC009054

This article is a companion to Shervais al. (2020), https://doi.org/10.1029/2020GC009093.

Key Points:

- Forearc basalts formed in response to subduction initiation by melting of depleted mantle after minor inputs of variably saline fluids
- Boninites were generated by melting residual mantle after fluxing by water rich melts from altered oceanic crust then crust and sediment
- The subducting plate melted at exceedingly shallow depths beneath oceanic crust being generated by seafloor spreading

Supporting Information:

- Supporting Information S1
- Table S1
- Table S2
- Table S3
- Table S4
- Table S5
- Figure S1

Correspondence to:
M. K. Reagan,
mark-reagan@uiowa.edu

Citation:
Coulthard, D. A., Reagan, M. K., Shimizu, K., Bindeman, I. N., Brounce, M., Almeev, R. R., et al. (2021). Magma source evolution following subduction initiation: Evidence from the element concentrations, stable isotope ratios, and water contents of volcanic glasses from the Bonin forearc (IODP expedition 352). *Geochemistry, Geophysics, Geosystems*, *22*, e2020GC009054. https://doi.org/10.1029/2020GC009054

Received 24 MAR 2020
Accepted 15 OCT 2020

© 2020. The Authors.
This is an open access article under the terms of the Creative Commons Attribution License, which permits use, distribution and reproduction in any medium, provided the original work is properly cited.

Magma Source Evolution Following Subduction Initiation: Evidence From the Element Concentrations, Stable Isotope Ratios, and Water Contents of Volcanic Glasses From the Bonin Forearc (IODP Expedition 352)

Daniel A. Coulthard Jr[1,2], Mark K. Reagan[1], Kenji Shimizu[3], Ilya N. Bindeman[4], Maryjo Brounce[5], Renat R. Almeev[6], Jeffrey Ryan[7], Timothy Chapman[8], John Shervais[9], and Julian A. Pearce[10]

[1]Department of Earth and Environmental Sciences, University of Iowa, Iowa City, IA, USA, [2]Now at Volcanic Risk Solutions, Massey University, Palmerston North, New Zealand, [3]Kochi Institute for Core Sample Research, Japan Agency for Marine-Earth Science and Technology, Nankoku, Kochi, Japan, [4]Department of Earth Sciences, University of Oregon, Eugene, OR, USA, [5]Department of Earth Science, University of California Riverside, Riverside, CA, USA, [6]Institüt Für Mineralogie, Leibniz Universität Hannover, Hannover, Germany, [7]School of Geosciences, University of South Florida, Tampa, FL, USA, [8]School of Environmental and Rural Science, University of New England, Armidale, NSW, Australia, [9]Department of Geology, Utah State University, Logan, UT, USA, [10]School of Earth & Ocean Sciences, Cardiff University, Cardiff, UK

Abstract International Ocean Discovery Program Expedition 352 to the Bonin forearc drilled the sequence of volcanic rocks erupted in the immediate aftermath of subduction initiation along the western margin of the Pacific Plate. Pristine volcanic glasses collected during this expedition were analyzed for major and trace elements, halogens, sulfur, and H and O isotopes with goals of characterizing the fluids and melts of subducted materials that were involved in generating the nascent upper plate crust. Incompatible trace element compositions of the oldest lavas (forearc basalts [FAB]) are similar to those of the most depleted mid-ocean ridge basalts globally. Most FAB were generated by decompression melting during seafloor spreading in a near-trench, supra-subduction zone environment with only minor involvement of diverse and generally dilute water-rich fluids from the subducting plate. Boninite series glasses are enriched in incompatible trace elements mobilized from the subducting plate, but strongly depleted in other elements, such as the middle-heavy rare-earth elements. These traits are attributed to generation of boninites largely by flux melting involving water-rich melts first derived from the leading edge of subducted basaltic crust and then from both subducted crust and sediment. These melts were generated at low pressures as the shallow, embryonic slab extracted heat from hot asthenosphere near the trench. The progressive depletion of the mantle source for the FAB-through-boninite sequence suggests that the asthenospheric mantle remained trapped above the nascent subducting plate for the first several million years of subduction beneath the Philippine Sea Plate.

Plain Language Summary The origin of crust created along the leading edge of the Philippine Sea Plate after the Pacific Plate began subducting beneath it about 52 million years ago was investigated by analyzing volcanic glasses recovered by drilling the Bonin forearc during International Ocean Discovery Program Expedition 352. The glasses have not been affected by alteration and thus preserve pristine compositions of the erupted lavas. Two deep water drill sites (U1440 and U1441) recovered basalts and rare andesites produced by crystal removal and crust assimilation. The compositions of the basalt glasses suggest that they were produced by depressurization of hot mantle during near-trench seafloor spreading in the presence of minor amounts of water-rich fluid from the newly subducting plate. Younger, more silica-rich lavas termed “boninites” were recovered from two sites drilled in shallower water (U1439 and U1442). Boninite glass compositions demonstrate that these boninites were generated when shallow hot mantle was invaded by water-rich melts derived first from the subducting basaltic crust and then this crust plus sediment.

1. Introduction

The inception of subduction beneath the Izu-Bonin-Mariana (IBM) intra-oceanic arc system was a significant tectonic event associated with a regional-to-global plate reorganization as well as the generation of significant new oceanic lithosphere in the western Pacific (e.g., M. K. Reagan et al., 2010, 2013; Stern & Bloomer, 1992). The resulting lithosphere is akin to that found in many supra-subduction zone ophiolites (e.g., Dilek & Furnes, 2009; J. A. Pearce & Robinson, 2010; J. W. Shervais, 1982, 2001). International Ocean Discovery Program (IODP) Expedition 352 drilled the volcanic stratigraphy of the nascent IBM crust (M. K. Reagan et al., 2015) for comparison with ophiolites and to understand better how subduction dynamically evolves. Published whole-rock analyses of Expedition 352 cores show that the oldest volcanic rocks in this sequence are basalts (M. K. Reagan et al., 2017; J. W. Shervais et al., 2019). These lavas have been termed fore-arc basalts (FAB) for their appearance in the modern forearc and to distinguish them from basalts generated in other tectonic settings (M. K. Reagan et al., 2010). Also prominent in the drill cores are magnesian andesitic rocks termed "boninite" after their type occurrence in the nearby Bonin Islands (e.g., Kuroda & Shiraki, 1975).

A primary goal of research on Expedition 352 cores has been to determine how magma genesis and seafloor dynamics changed over time in response to subduction initiation. Critically important in this effort is ascertaining the relative contributions of mantle and subducted sources to magmas, which requires precise determination of ratios between elements that are mobilized from subducting slabs to different degrees. Prior work in the IBM forearc has shown that boninite volcanism succeeded FAB volcanism as seafloor spreading waned and the protoarc was established (Ishizuka et al., 2011; M. K. Reagan et al., 2019). Trace elements that are both incompatible in magmas and relatively insoluble in aqueous fluids, such as rare-earth elements (REE) and some high field strength elements (HFSE; e.g., Ti, Y, Nb, Ta), were shown to be strongly depleted in FAB (M. K. Reagan et al., 2010; J. W. Shervais et al., 2019) and even more depleted in boninites (e.g., P. F. Dobson et al., 2006; Y. B. Li et al., 2013; J. W. Shervais et al., 2020; R. N. Taylor et al., 1994).

Quantifying the original concentrations of subduction-mobile elements in Expedition 352 lavas has, however, been challenging because of hydrothermal alteration and sea-floor weathering (M. K. Reagan et al., 2015). Although sampling for the whole rock geochemical studies of Expedition 352 cores cited above targeted least altered whole rocks, even incipient alteration may affect the concentrations of fluid-soluble elements such as K, Rb, Cs, U, Ba, Sr, and Pb. Such alteration may mask primary trends in trace element compositions, especially in highly depleted lavas like those found in the IBM forearc (e.g., Ishizuka et al., 2011; M. K. Reagan et al., 2010; J. W. Shervais et al., 2019). Fortunately, Expedition 352 drilling recovered scores of volcanic glasses that have preserved the pristine compositions of the quenched basalt and boninite melts.

For this work, we have analyzed 147 glass fragments for major element compositions. Subsets of these glasses were analyzed for trace element concentrations and O and H isotopic compositions. The overarching goal has been to provide an accurate and comprehensive petrogenetic history of the modern IBM forearc crust. Specifically, we have addressed when and how aqueous fluids and melts from the subducting Pacific plate became involved in generating the first IBM crust.

2. Background

The Philippine Sea Plate stretches ~3,000 km south from Japan to Palau, and west from the IBM trench to Taiwan and the Ryuku and Philippine trenches (Figure 1). The oldest terranes of the Philippine Sea Plate are Mesozoic crustal fragments, including the Huatung basin near Taiwan (131-119 Ma, Deschamps et al., 2000), remnant arcs and ocean islands of the Oki-Daito Ridge, the Daito Ridge, and the Amami Plateau (120-115 Ma, Hickey-Vargas et al., 2005; Ishizuka et al., 2013) in the north, and the Palau Basin to the south (B. Taylor & Goodliffe, 2004). Mesozoic basalt was recovered from the Bonin trench wall at 27.3°N latitude (159 Ma, Ishizuka et al., 2011a). Sedimentary rocks of Valanginian to Cenomanian age (138-97 Ma) were recovered at 19.4°N from the Mariana inner trench wall (Johnson et al., 1991).

Subduction of the Pacific Plate beneath the assembled Mesozoic terranes began between 51.9 and 52.5 Ma (M. K. Reagan et al., 2019). Subsequent near-trench spreading generated the FAB then boninite crust that is preserved along the present tectonic margin. Shinkai 6500 diving in the Izu and Bonin forearcs between 32°

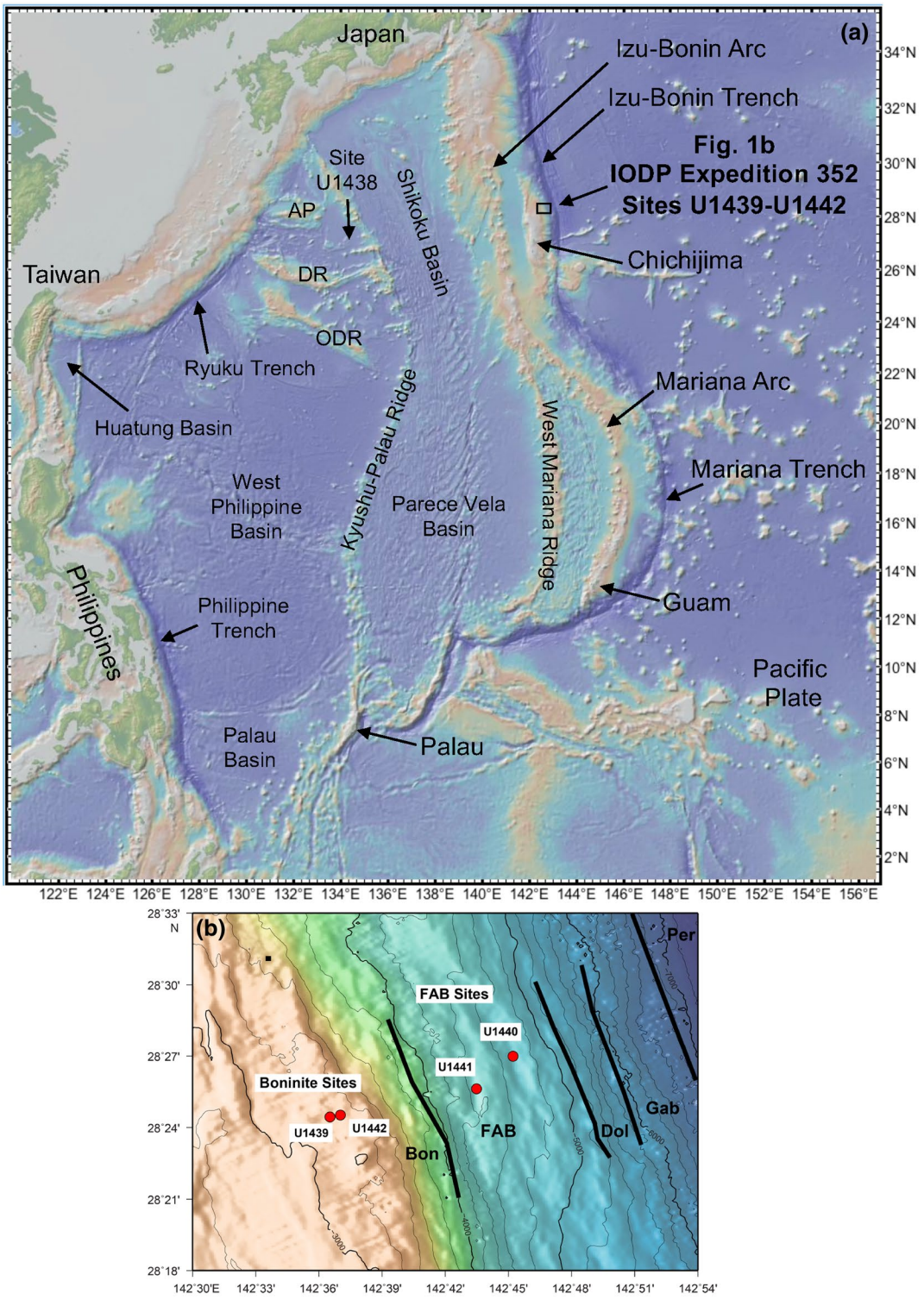


Figure 1. (a) Bathymetric map from GeoMapApp (http://www.geomapapp.org; W. B. F. Ryan et al., 2009) illustrating features of the Philippine Sea Plate and surrounding areas. (b) Location map for IODP Expedition 352 drill sites. AP, Amami Plateau; DR, Daito Ridge; IODP, International Ocean Discovery Program; ODR, Oki-Daito Ridge.

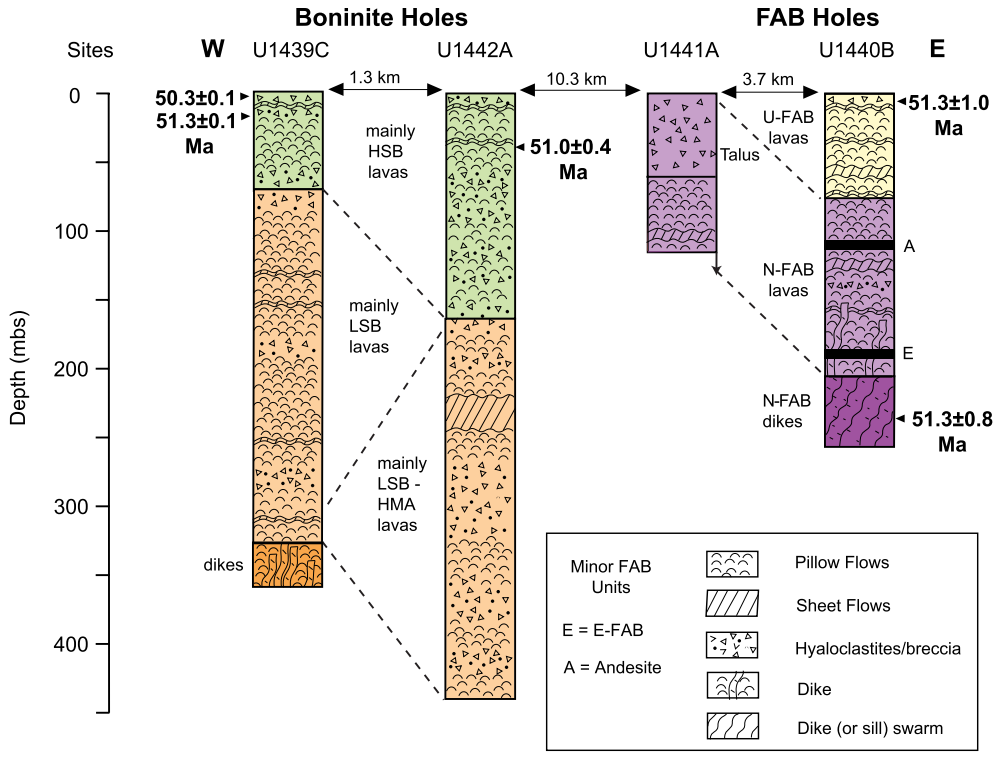


Figure 2. Simplified stratigraphic columns for the principal basement penetrating holes drilled during IODP Expedition 352 after M. K. Reagan et al. (2015) and H. Y. Li et al. (2019). Locations for the highest quality $^{40}Ar/^{39}Ar$ ages from M. K. Reagan et al. (2019) are shown by arrowheads next to the columns. Also shown are approximate trench-normal distances between holes. FAB, forearc basalt (U, upper; N, normal; E, enriched); HMA, high-Mg andesite; HSB, high-Si boninite; LSB, low-Si boninite.

and 27°N latitude (DeBari et al., 1999; Ishizuka et al., 2011) and in the forearc south of Guam at 12°N (M. K. Reagan et al., 2010) have identified and sampled these volcanic sequences.

During Expedition 352, drilling at two deep water sites (U1440 and U1441) recovered cores of FAB and related hypabyssal intrusive rocks (Figure 2). Most FAB glass samples analyzed in this study are from Hole U1440B (28°26.9976'N, 142°45.2244'E; 4,775 m water depth), which penetrated a thick sequence of lavas, predominantly basalts but including FAB-related andesites. The hole terminated in dolerites inferred to be the top of the underlying shallow intrusive complex that fed the volcanic system. Two analyzed glass samples are from Hole U1441A (28°25.6379'N, 142°43.5390'E; 4,447 m water depth), which had limited penetration into basement (M. K. Reagan et al., 2015).

FAB lavas from Hole U1440B have been divided into subunits by compositional trends correlated to stratigraphic position (H. Y. Li et al., 2019; J. W. Shervais et al., 2019). The lower lavas are interpreted to have erupted at a spreading axis (Figure 2) based on their geochemical ties to the underlying dolerites, which are thought to represent a sheeted dike complex (M. K. Reagan et al., 2017). These axial lavas are further divided into normal FAB (N-FAB) and rare enriched FAB (E-FAB), which are compositionally distinct. Glasses from Hole U1441A are axial N-FAB lavas. A FAB-related andesite vitrophyre lies near the top of the axial FAB in Hole U1440B (M. K. Reagan et al., 2017). The basalt glasses found above this andesite are termed "upper" FAB (U-FAB). Compositional distinctions between U-FAB and N-FAB led J. W. Shervais et al. (2019) and H. Y. Li et al. (2019) to conclude that these lavas were erupted in an off-axis setting. Regardless, many compositional traits for U-FAB overlap with N-FAB and, when this is true in the discussion below, FAB is used as the general acronym applying to both lava types.

Boninites were encountered at Sites U1439 (28°24.4491'N, 142°36.5368'E; 3,129 m water depth) and U1442 (28°24.5784'N, 142°37.3368'E; 3,162 m water depth). The SiO_2, MgO, and TiO_2 concentrations in whole rocks have been used to distinguish boninite lineages (Figure 3) using the classification scheme proposed

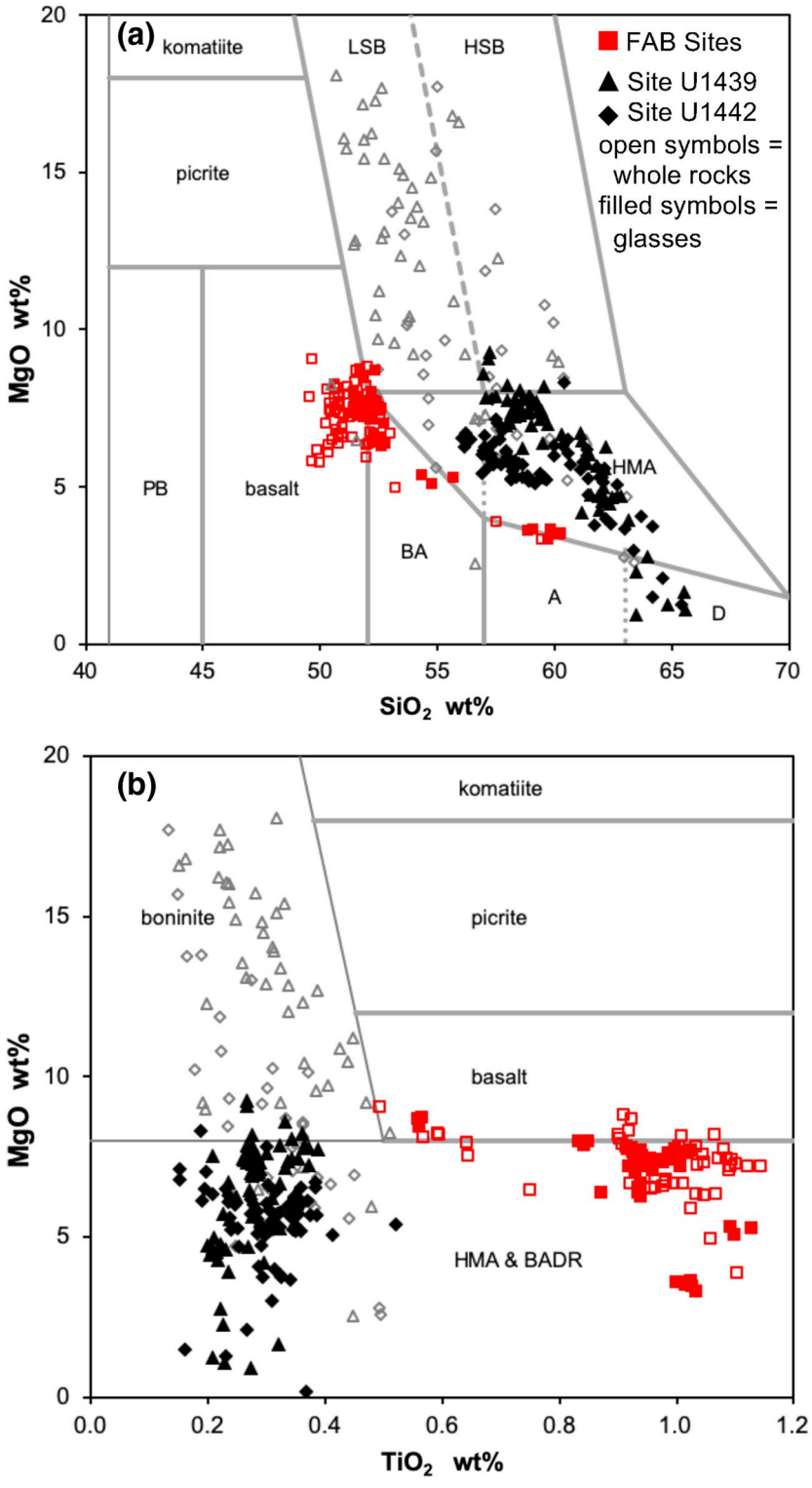


Figure 3. Boninite classification plots using methods and division definitions from J. A. Pearce and Reagan (2019). (a) MgO versus SiO_2. (b) MgO versus TiO_2. Note the overlap in FAB glass and whole-rock compositions, but the greater degree of differentiation for boninite glasses compared with whole rocks. Whole-rock data are from Shervais et al. (2019). A, andesite; BA, basaltic andesite; BADR, basalt-andesite-dacite-rhyolite series; D, dacite; FAB, forearc basalt; HMA, high-Mg andesite; HSB, high-Si boninite; LSB, low-Si boninite; PB, picrobasalt.

by J. A. Pearce and Reagan (2019). Based on this scheme, low-Si boninites (LSB) have SiO_2 concentrations varying from 52 to 57 wt.% at 8 wt.% MgO, whereas high-Si boninites (HSB) have 57 to 63 wt.% SiO_2 at 8 wt.% MgO. Boninites with higher MgO concentrations for both series plot toward the compositions of olivine and orthopyroxene, which are the early crystallizing phases. Differentiated boninite-series lavas with <8 wt.% MgO are termed high-Mg andesites (HMA) or andesites depending on their precise MgO and SiO_2 concentrations (J. A. Pearce and Reagan, 2019).

Sites U1439 and U1442 both have a stratigraphy of variably differentiated HSB overlying LSB and LSB-related HMA (Figure 2 and Shervais et al., 2020). HSB in Hole U1439C were drilled between 182 and 251 m below sea floor (mbsf) or 0–69 m below sediment (mbs), with underlying LSB extending to a depth of about 523 mbsf (341 mbs). About 10 m of HMA follow, and the hole terminates at 542 mbsf (360 mbs) in a sequence of interspersed HMA lavas and LSB-related dolerites (M. K. Reagan et al., 2015). The latter were inferred to be related to the shallow feeder system for overlying LSB (M. K. Reagan et al., 2015). In Hole U1442A, HSB were encountered between 84 and 250 mbsf (0–166 mbs), with a sequence consisting largely of LSB-related HMA extending from 250 mbsf to the bottom of the hole at 523 mbsf (439 mbs, Figure 2). Based on these characteristics, and stratigraphically correlated geochemical observations common to both Holes U1439C and U1442A, M. K. Reagan et al. (2017) concluded that LSB were generated while seafloor spreading was ongoing, whereas HSB generation was attributed to the beginning of "focused magmatism" related to the beginning of the protoarc/early arc stage, marking the time at which seafloor spreading slowed or ceased. This was based on an abrupt shift to more siliceous compositions that was identified at shallow levels in Holes U1439C and U1442A. This shift also is associated with an apparent change in the rate of migration of volcanic centers away from the trench (M. K. Reagan et al., 2019) and a change in isotopic compositions (H. Y. Li et al., 2019). Note that the stratigraphic boundary between LSB and HSB for Hole U1442A, as presented in Figure 2, is a slight revision of that presented in M. K. Reagan et al. (2015). This change was made necessary by our postcruise analyses (Shervais et al., 2020).

Compiled $^{40}Ar/^{39}Ar$ and U-Pb zircon ages (M. K. Reagan et al., 2019 and references therein) show that seafloor spreading and production of FAB to LSB crust took place between 52.5 and 51.3 Ma. HSB volcanism associated with the embryonic arc began at c. 51.3 Ma and persisted until about 46 Ma, as the arc moved westward on the Bonin Ridge. The transition from boninite to tholeiitic and calc-alkaline arc volcanism in what is now the Bonin forearc began at about 46 Ma and was complete by about 44 Ma (Ishizuka et al., 2006, 2011, 2020).

3. Samples and Methods

3.1. IODP Samples and Preparation

Fresh glass from all volcanic lithologies were recovered during Expedition 352. FAB glasses were largely sourced from chilled margins of pillow lavas, whereas many of the boninite glasses were sampled from hyaloclastites (Figure S1). Optically fresh FAB glasses are generally aphyric, with rare plagioclase and/or clinopyroxene phenocrysts present in some samples. They typically contain a few percent of vesicles. These vesicles and fractures often are lined with calcite or zeolites and rarely contain pyrite and native copper. Many FAB glasses have millimeter to sub-millimeter scale, cryptocrystalline, stony spherules, which we interpret to have resulted from devitrification (M. K. Reagan et al., 2015). E-FAB Core U1440B 30R-1 is noteworthy in its high abundance of vesicular enclaves (M. K. Reagan et al., 2015). The FAB-related andesite from Core U1440B 19R-1 is a spherulitic vitrophyre that lacks vesicles. Analyses were performed on glass fragments chosen to avoid the spherules. Sample U1440B 9G consists of glass fragments from a "ghost core," which comprises material drilled through after a hole collapse. This sample could thus represent glasses from the level of the base of the collapsed material (~144 mbsf) to the top of the basement section at 115 mbsf.

Glassy LSB samples are greenish gray to faintly brown. They are porphyritic with olivine and chromite phenocrysts, as well as quench-textured clinopyroxene and/or plagioclase. Orthopyroxene, clinopyroxene, and plagioclase phenocrysts are also present in some differentiated samples (Figure S1). Glassy HSB are greenish to lilac gray, and porphyritic with phenocrysts of orthopyroxene ± olivine ± chromite and quench-textured orthopyroxene and clinopyroxene. Rhyolitic samples with HSB lineage have groundmass plagioclase.

Boninites are characteristically vesicular, with zeolites, calcite, clays, and rare sulfides commonly lining or filling veins and vesicles (M. K. Reagan et al., 2015).

3.2. Microanalytical Techniques

Optically fresh glass was used for all major and trace element analyses. Great care was taken to avoid samples with spherules and/or microlites, and samples with evidence of alteration (i.e., devitrified/palagonitized glass fragments) were disregarded.

Details of the analytical techniques at each laboratory may be found in the supporting information. Briefly, major element compositions were obtained at the University of Iowa (lab. A) on a JEOL JXA-8230 Superprobe electron probe microanalyzer (EPMA) with five wavelength-dispersive spectrometers employing eight large-format diffracting crystals, at Japan Agency for Marine-Earth Science and Technology (JAMSTEC; lab. B) using field emission EPMA (JEOL JXA-8500F), and at the Institute of Mineralogy, Leibniz University Hannover (lab. C) using a Cameca SX100. Analyses of overlapping core intervals by labs A, B, and C (e.g., samples U1440B 9G, U1440B 12R-2 67/69, U1440B 20R-1 53/54, U1440B 23R-1 76/78, U1440B 31R-1 63/89, U1439C 19R-4 84/90, U1442A 17R-1 61/65, U1442A 26R-1 54/58) show inter-laboratory consistency for major elements within analytical errors as demonstrated by repeat analyses of standards BCR-2G, BHVO-2G, and VG-A99 by lab. A (Table S1). Trace element compositions of glasses were determined at lab. A by LA ICP-MS using a NewWave 213 nm laser connected to a Thermo X-Series II Quadrupole ICP-MS. ^{43}Ca was used as a normalizing isotope and BHVO-2G as the calibration standard. Accuracy and precision for each element are illustrated by repeat analysis of BCR-2G and reported in Table S1. P_2O_5, F, Cl, and S content of glass were determined by secondary ion mass spectrometry (SIMS; AMETEK-CAMECA ims-1280HR) at JAMSTEC, following the methods of Shimizu et al. (2017).

3.3. Stable Isotope and Water Analysis

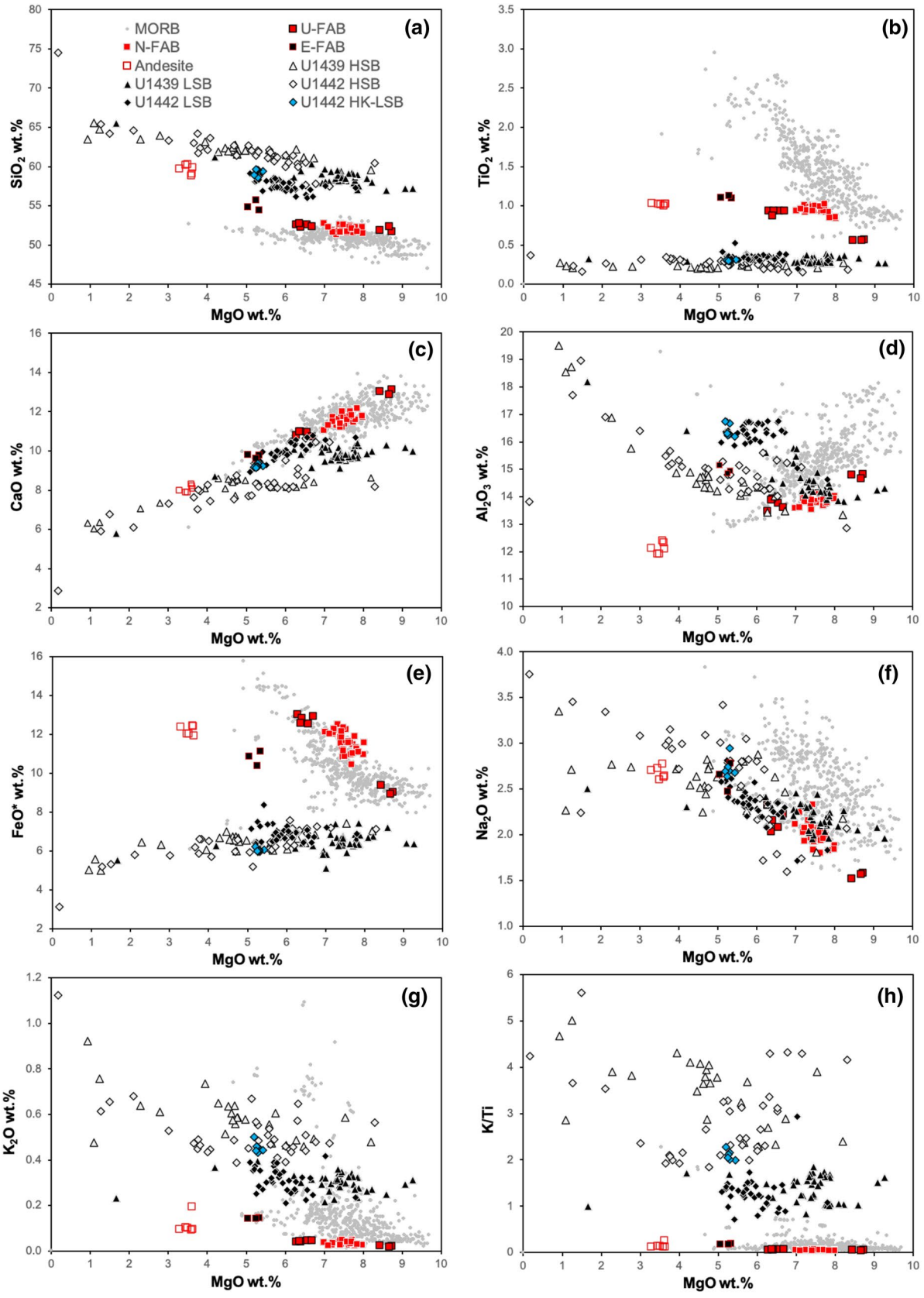
Fresh glass fragments, generally between 0.2 and 1.5 mm in length, were hand-picked for stable isotope analysis. Every effort was made to select samples that showed no alteration and minimal crystal content. For FAB, this meant that samples were aphyric, and lacked surficial alteration products. Although the presence of stony spherules was minimized by hand-picking, they could not be entirely avoided in samples U1440B 19R-1 14/15, U1440B 20R-1 53/54, and U1440B 31R-1 63/68. Optical examination revealed that the spherules constituted less than 20% of these analyzed samples. Boninite fragments were typically glass with embedded microphenocrysts (c. 1%–15%), and thus the stable isotope data represent more of a whole rock than a glass composition. Although vesicles were avoided during hand-picking, it is possible that glass fragment interiors had some vesicles. In addition, analyzed glass fragments from Samples U1442 49R-2 69/72 and U1442A 56R-2 24/27 contained some perlitic fractures.

Total H_2O, bulk $\delta^{18}O$, and water-in-glass δD measurements were conducted on a gas source MAT 253 isotope ratio mass spectrometer at the University of Oregon using the TCEA and laser fluorination methods described in Bindeman et al. (2012), Martin et al. (2017), and Loewen et al. (2019). Water was determined with a precision of ±0.02–0.05 wt.%; the precision for δD was ±1‰–2‰ (1σ). Additional details may be found in the supporting information.

4. Results

4.1. Major and Trace Element Compositions—FAB

Because of their low crystallinity, FAB glasses have chemical compositions similar to those of FAB whole rocks (Figure 3). N-FAB are modestly differentiated, containing 51.1–52.1 wt.% SiO_2, 10.8–12.2 wt.% FeO^*, 11.1–12.0 wt.% CaO, and 7.0–7.7 wt.% MgO. U-FAB glasses have major element-oxide compositions similar to those of N-FAB, but they are more variably differentiated with ~52 wt.% SiO_2, 9–13 wt.% FeO^*, 11–13 wt.% CaO, and MgO = 6.2–8.7 wt.% (Table S1; Figure 4). Glasses from the U-FAB ghost core (U1440B 9G) were found to have a restricted range in composition based on 266 individual analyses of dozens of


(a)
MORB
N-FAB
Andesite
U1439 LSB
U1442 LSB
U-FAB
E-FAB
U1439 HSB
U1442 HSB
U1442 HK-LSB
SiO2 wt.%
MgO wt.%
(b)
TiO2 wt.%
MgO wt.%
(c)
CaO wt.%
MgO wt.%
(d)
Al2O3 wt.%
MgO wt.%
(e)
FeO* wt.%
MgO wt.%
(f)
Na2O wt.%
MgO wt.%
(g)
K2O wt.%
MgO wt.%
(h)
K/Ti
MgO wt.%

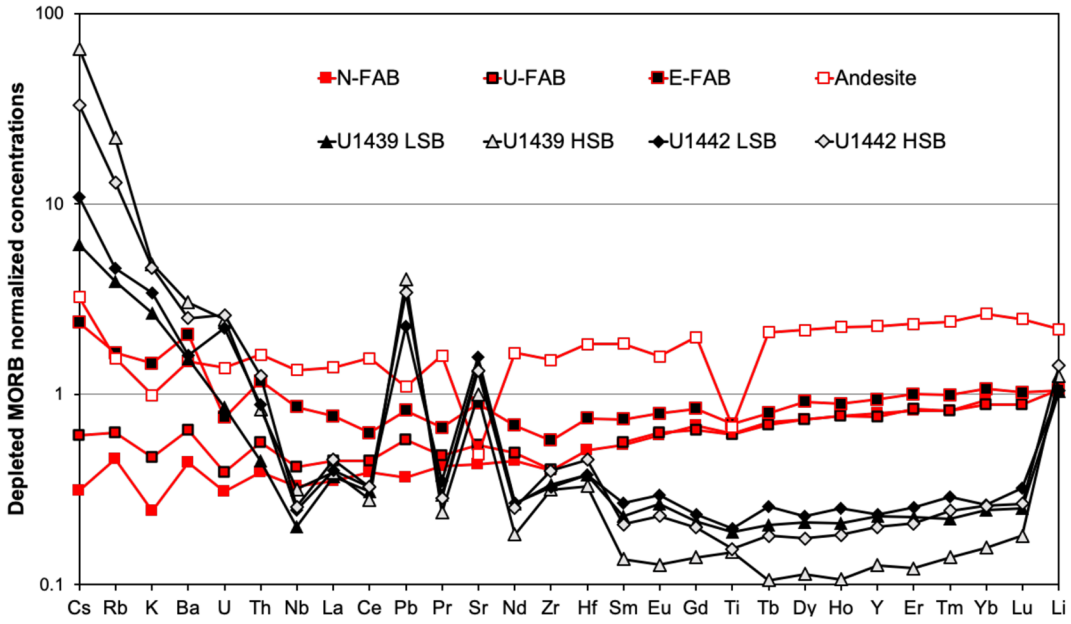


Figure 5. Representative incompatible trace element concentrations for volcanic glasses recovered during IODP Expedition 352 normalized to the average depleted MORB (DMORB) composition from Gale et al. (2013). N-FAB = Core U1440B-24R-1 48/50; U-FAB = Ghost Core U1440B-9G average; E-FAB = Core U1440B-30R-1 19/21; FAB Andesite = Core U1440B-19R-1 14/15; U1439 LSB = Core U1439C-28R-2 93/95; U1439 HSB = Core U1439A-21X-CC 22/25; U1442 LSB = Core U1442A-55R-1 68/72; U1442 HSB = Core U1442A-10R-3 82/90. FAB, forearc basalts; IODP, International Ocean Discovery Program; MORB, mid-ocean ridge basalt.

fragments (Table S2), which we take to mean that all fragments represent one eruptive unit. FAB glasses have exceedingly low K_2O concentrations (0.02–0.07 wt.%), in marked contrast to whole rocks which have K_2O concentrations mostly above 0.1 wt.% ranging up to 0.9 wt.% (J. W. Shervais et al., 2019). Indeed, only one of 35 whole-rock samples reported in J. W. Shervais et al. (2019) has a K_2O concentration within the range of those for the glasses. These observations illustrate that nearly all FAB whole rocks have undergone secondary enrichment in potassium.

The E-FAB glasses are basaltic andesites, with $SiO_2 \simeq 53$ wt.%, CaO ≃ 9.4 wt.%, MgO ≃ 5.2 wt.%, and significantly higher K_2O concentrations compared with other FAB (0.14 wt.%). The andesite glasses have ∼59 wt.% SiO_2, 3.2–3.6 wt.% MgO, and 7.7–8.1 wt.% CaO. K_2O concentrations in the andesites are higher than those in FAB by factors of 2–10 (Figure 4). Positive Al_2O_3-MgO and CaO-MgO correlations in FAB and andesite glasses are consistent with differentiation resulting largely, but not entirely, from plagioclase and clinopyroxene fractionation from parental basalts with a narrow range in composition (see below). TiO_2 and FeO^* concentrations in the andesites lie off of the main N-FAB trends because of magnetite fractionation.

In comparison with mid-ocean ridge basalt (MORB) glasses (Jenner & O'Neill, 2012), FAB glasses have lower TiO_2, Na_2O, and K_2O and higher SiO_2 and FeO^* at a given MgO concentration (Figure 4). Al_2O_3 is lower than MORB in most FAB. However, E-FAB has relatively high concentrations of Al_2O_3 for its degree of differentiation, the likely consequence of suppression of plagioclase crystallization due to its high water content (see below). Only on plots of CaO versus MgO and MnO versus MgO (not shown) do FAB and MORB glasses overlap.

Incompatible trace element patterns for FAB glasses resemble those of the most depleted MORB found anywhere on Earth (Figure 5). E-FAB are enriched in highly incompatible trace elements compared with other FAB. Incompatible trace element concentrations are high in the FAB-related andesites, with patterns

Figure 4. Concentrations of selected oxide concentrations (a)–(g) and K/Ti (h) ratios plotted against MgO concentrations for IODP Expedition 352 glasses. Data for MORB are glasses erupted at spreading centers from Jenner and O'Neill (2012). Data are normalized to 100% oxide totals. See text for explanation of rock classification. IODP, International Ocean Discovery Program; MORB, mid-ocean ridge basalt.

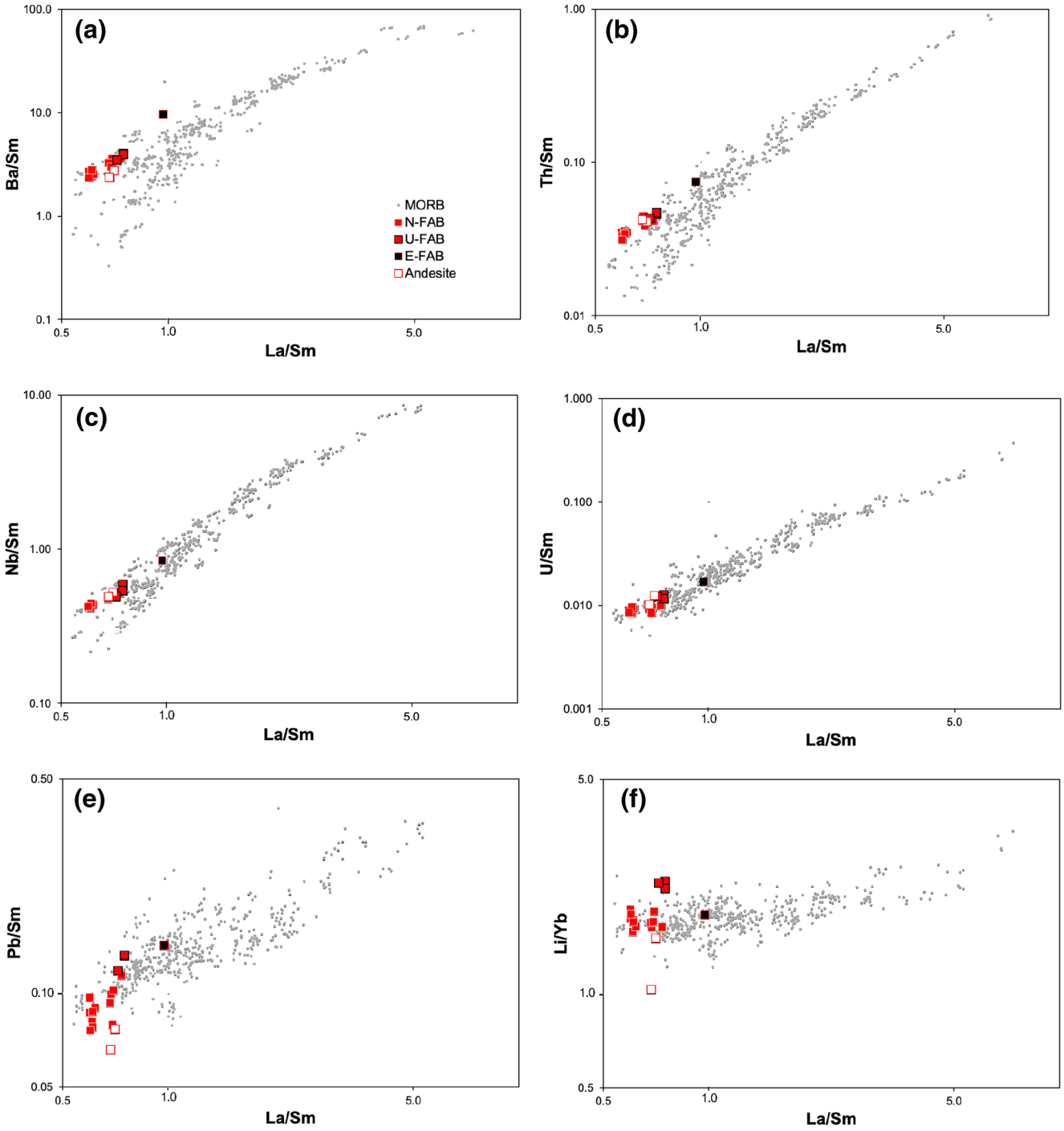


Figure 6. Logarithmic plots of incompatible trace element ratios for FAB glasses versus La/Sm. MORB data represent glasses erupted at spreading centers from Jenner and O'Neill (2012). FAB, forearc basalts; MORB, mid-ocean ridge basalt.

generally parallel to, and above, those of FAB. Exceptions include Sr + Eu, Ti, and Pb, which are depleted as a result of plagioclase, magnetite, and sulfide fractionation respectively.

The incompatible element depletion in FAB glasses is further illustrated in Figure 6, which presents plots of highly incompatible elements relative to Sm for FAB glasses, as well as for glasses from the MORB database (Jenner & O'Neill, 2012). These ratios are plotted against La/Sm, which is used as a measure of source

depletion. Sm is chosen as the denominator as it is one of the least subduction-mobile elements measured. On these plots, MORB glasses form arrays with gradients which reflect the compatibilities of the plotted elements relative to La such that "enriched" MORB have high ratios and "depleted" MORB have low ratios. Subduction inputs lead to compositions that plot above the MORB arrays for subduction-mobile elements such as U, Pb, and Ba.

The key observation for Figure 6 is that the FAB glass compositions lie at the low-La/Sm end of the arrays reflecting their aforementioned depletions. They also lie within the MORB array indicating minimal subduction additions. Some element concentrations relative to Sm in FAB (e.g., Ba, Th, and Nb) lie along the upper edge of the MORB array. This is a characteristic of Philippine Sea Plate basalts in general (Hickey-Vargas, 1998; J. A. Pearce et al., 1999), including those from the IBM forearc (Ishizuka et al., 2011; H. Y. Li et al., 2019; M. K. Reagan et al., 2010).

Although U-FAB plot along the same trends as N-FAB, Pb/Sm and Li/Yb ratios are higher for U-FAB than for N-FAB or MORB (Figures 6e and 6f). The E-FAB glass is measurably enriched in some subduction-mobile elements compared with MORB (e.g., Ba/Sm; Figure 6a). Nevertheless, many other elements characteristically mobilized from subducting plates are not significantly enriched in U-FAB or E-FAB (e.g., U, Pb; Figures 6d and 6e).

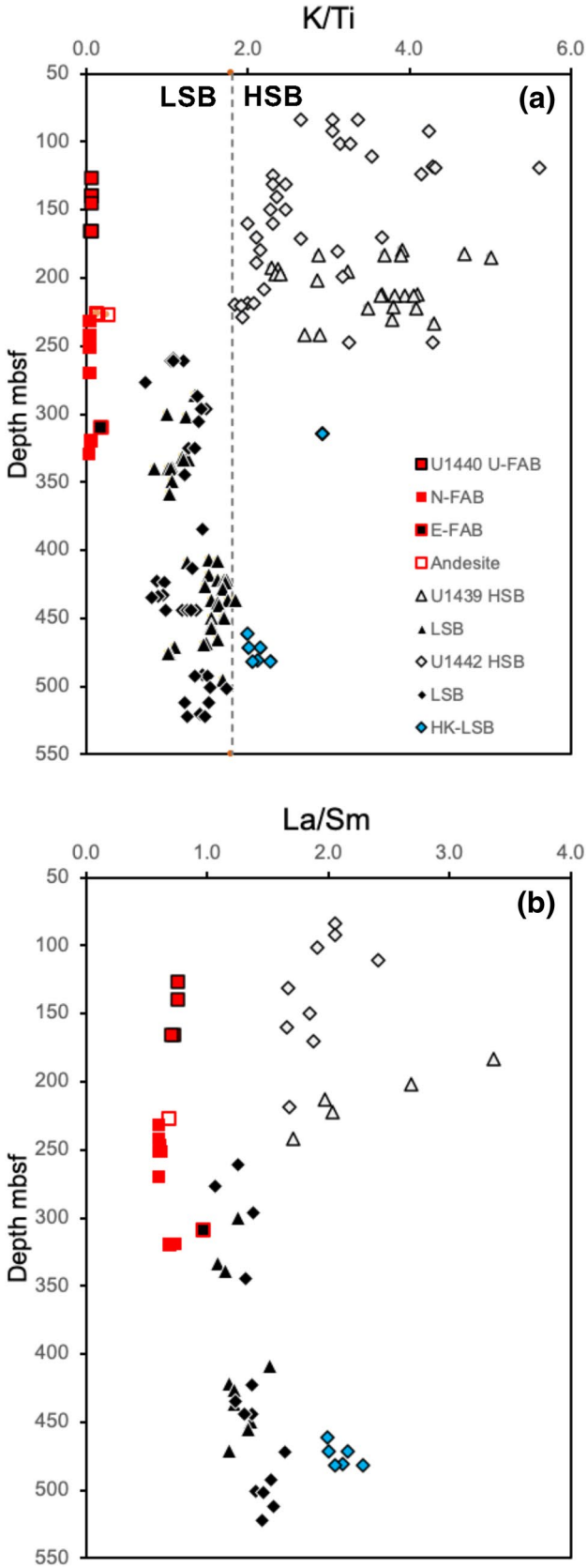
Ti/V for FAB are higher than those for MORB, an observation consistent with FAB from other locations in the IBM forearc (M. K. Reagan et al., 2010). This is mostly a reflection of relatively low concentrations of TiO_2 in FAB, without concomitantly low V concentrations. The FAB-related andesite has low V concentrations with respect to FAB, but similar TiO_2 concentrations, which is likely the result of clinopyroxene and magnetite fractionation. Cr concentrations are generally low in FAB relative to MORB, with N-FAB having Cr concentrations between 79 and 236 ppm. The relatively differentiated E-FAB and the FAB-related andesite have 31–43 ppm Cr (Table S1).

4.2. Major and Trace Element Compositions—Boninite Series

Nearly all boninite series glasses analyzed here have less than 8 wt.% MgO and one has more than 0.5 wt.% TiO_2 (Table S1; Figure 3). These glasses thus plot within the HMA and andesite fields on the classification diagrams of J. A. Pearce and Reagan (2019). The differentiated nature of the glasses requires the use of incompatible trace element ratios, as well as stratigraphic correlations to whole-rock data to distinguish LSB and HSB lineages. Onboard Expedition 352, Ti/Zr ratios analyzed by portable X-ray fluorescence analysis of whole rocks were used to aid discrimination between LSB and HSB (Ryan et al., 2017). Here, the pristine nature of the glasses allows a wider choice of trace element ratios to discriminate glass compositions, including elements that are mobile during alteration of whole rocks (e.g., K, Cs, Rb, Sr, Pb, and U).

Because not all glasses were analyzed for trace elements, we chose the minor element ratio, K/Ti, to distinguish HSB series from LSB series glasses. The K/Ti ratio of 1.8 provides a discriminant which gives a HSB-LSB boundary that corresponds well to the depth of the boundary obtained for whole rocks using the MgO-SiO_2-TiO_2 classification of J. A. Pearce and Reagan (2019). For example, the whole rocks recovered from Hole U1439C above 251 mbsf are HSB (or HMA with HSB lineage; see Shervais et al., 2020) based on the MgO-SiO_2-TiO_2 classification and all glasses above this level have $K/Ti > 1.8$. Correspondingly, whole rocks below 251 mbsf are LSB or LSB-related HMA and glasses have $K/Ti < 1.8$ (Figure 7). Similarly, for Hole U1442A, whole rocks above 250 mbsf are of the HSB lineage and glasses have $K/Ti > 1.8$, whereas whole rocks below 250 mbsf have a LSB lineage (Shervais et al., 2020) and most have $K/Ti < 1.8$. However, there are exceptions for Hole U1442A. These include glasses from 315 and 450–490 mbsf, which have higher K/Ti but major element compositional traits (such as high Al_2O_3) more in keeping with LSB (Figure 4). These glasses are assigned to a separate high-K, low-Si boninite (HK-LSB) series on compositional diagrams as they appear to represent an important end-member composition for both LSB and HSB series lavas (see below).

HSB series glasses from Sites U1439 and U1442 are more evolved than equivalent whole rocks (Figure 3), reflecting the high crystal contents of boninite lavas (M. K. Reagan et al., 2015; Whattam et al., 2020). This also is true for most LSB series glasses from Site U1439. Glass and whole-rock compositions for Hole U1442,


K/Ti
0.0
2.0
4.0
6.0
LSB
HSB
(a)
Depth mbsf
50
100
150
200
250
300
350
400
450
500
550
U1440 U-FAB
N-FAB
E-FAB
Andesite
U1439 HSB
LSB
U1442 HSB
LSB
HK-LSB
La/Sm
0.0
1.0
2.0
3.0
4.0
(b)

which is characterized by a thick section of HMA at its base (M. K. Reagan et al., 2017), exhibit greater overlap and, in general, LSB series glasses from Hole U1442A have more evolved compositions than those from Hole U1439C (Figure 4). LSB series glasses from Sites U1439 and U1442 also follow somewhat separate fractionation trends, with Site U1439 glasses having higher SiO_2 and CaO concentrations at a given MgO concentration compared with glasses from Site U1442.

Compositions of HSB series glasses from Sites U1439 and U1442 exhibit considerable overlap. In particular, they are both ubiquitously evolved as reflected in their low MgO concentrations (Figure 4). This greater degree of fractionation for HSB series glasses compared with LSB series glasses is not observed for whole-rock compositions (Figure 3) and this reflects the porphyritic nature of HSB (Whattam et al., 2020). The LSB glasses from Site U1439 are generally less evolved than LSB from Site U1442. In addition, Site U1439 LSB glasses lie on a linear extrapolation of the HSB trend for SiO_2 (Figure 4a), whereas Site U1442 glasses are displaced to lower SiO_2. For boninite series samples with greater than 4 wt.% MgO, HSB series glasses generally have low concentrations of CaO and Al_2O_3 compared with similarly fractionated LSB series glasses (Figures 4c and 4d), and they generally fall within the low-Ca lineage of Crawford et al. (1989). At lower MgO concentrations, all boninite-series samples have CaO concentrations that plot along an overall FAB-MORB trend. FeO* concentrations are broadly constant at about 5.5–6.5 wt.% for all boninite series glasses down to c. 4 wt.% MgO, below which FeO* begins to decrease together with MgO (Figure 4e). Distinct differences between LSB and HSB series glasses are illustrated in Figures 4g and 4h, where (with the exception of HK-LSB) K_2O concentrations and K/Ti are, on average, higher in HSB than LSB.

Middle and heavy REE concentrations are lower in boninite series glasses than in FAB glasses (Figure 5). These concentrations are lowest in HSB, approaching those of primitive mantle even in these relatively differentiated glasses. Normalized light REE concentrations are roughly the same as, or slightly depleted relative to, the middle REE in LSB series glasses, whereas normalized LREE concentrations are enriched over MREE in HSB series glasses. This includes the one HK-LSB series glass analyzed for trace elements (U1442A 52R-1 36/43).

Nb, Ti, and Y are strongly depleted in boninite series glasses compared to MORB and FAB (Figure 5), whereas Zr and Hf have concentrations that are similar to, or somewhat lower than, those of FAB. This results in a significant enrichment of these elements compared to the middle REE in all Expedition 352 boninites, particularly HSB. This is consistent with other boninites from the IBM forearc (e.g., Ishizuka et al., 2006; H. Y. Li et al., 2019; J. A. Pearce et al., 1992; M. K. Reagan et al., 2010) and some (e.g., Cape Vogel: Kamenetsky et al., 2002; Kudi: Yuan et al., 2005; Thetford Mines: Pagé et al., 2009) but not all (e.g., Oman: Godard et al., 2003; Troodos: Woelki et al., 2018) ophiolites.

All boninite series glasses are enriched in certain highly incompatible trace elements (e.g., Cs, Rb, K, Sr, Ba, Pb, Th, U, and Li) relative to the REE when compared with FAB and MORB glasses (Figures 5, 8, and 9). We term these "fluid-mobile elements" because these elements are commonly transferred from subducting slabs to arc magma sources in water-rich fluids and melts (e.g., Schmidt & Jagoutz, 2017; J. W. Shervais & Jean, 2012). Enrichments in fluid-mobile elements are anticorrelated with REE concentrations, resulting in high Rb/Sm for HSB series glasses compared with LSB series glasses (Figure 8a). These enrichments are also shared by whole-rock compositions, although ratios between more and less fluid-mobile elements are more variable in whole rocks (cf. Shervais et al., 2020). HSB and LSB series glasses have different compositional trajectories on plots utilizing ratios between fluid-mobile elements and REE (e.g., Ba/Sm vs. Rb/Sm, Figure 8a; Li/Yb vs. Dy/Yb, Figure 9a), illustrating that the compositions of the slab-derived fluids/melts involved in flux melting differ for HSB and LSB (see also H. Y. Li et al., 2019).

In addition, REE patterns for LSB and HSB series glasses drilled at Site U1439 differ subtly from equivalents drilled at Site U1442 (e.g., La/Sm is on average higher in Site U1439 glasses than in Site U1442 glasses; Figure 8c). At both boninite sites, incompatible trace element ratios in LSB series glasses, such as La/Sm and

Figure 7. (a) Plot of K/Ti versus depth of basement cores in meters below the sea floor (mbsf) for FAB and FAB-related glasses from site U1440 and boninites recovered from sites U1439 and U1442. K/Ti = 1.8 generally discriminates between low-Si and high-Si boninites, although there are rare LSB from Site U1442 with K/Ti values overlapping with those of HSB. These are discriminated as high-K, low-Si boninites (HK-LSB). (b) Plot of La/Sm versus depth. Note that incompatible trace element abundances in LSB become more FAB-like upsection, whereas HSB compositions generally become less FAB-like upsection. FAB, forearc basalts; HSB, high-Si boninites; LSB, low-Si boninites.

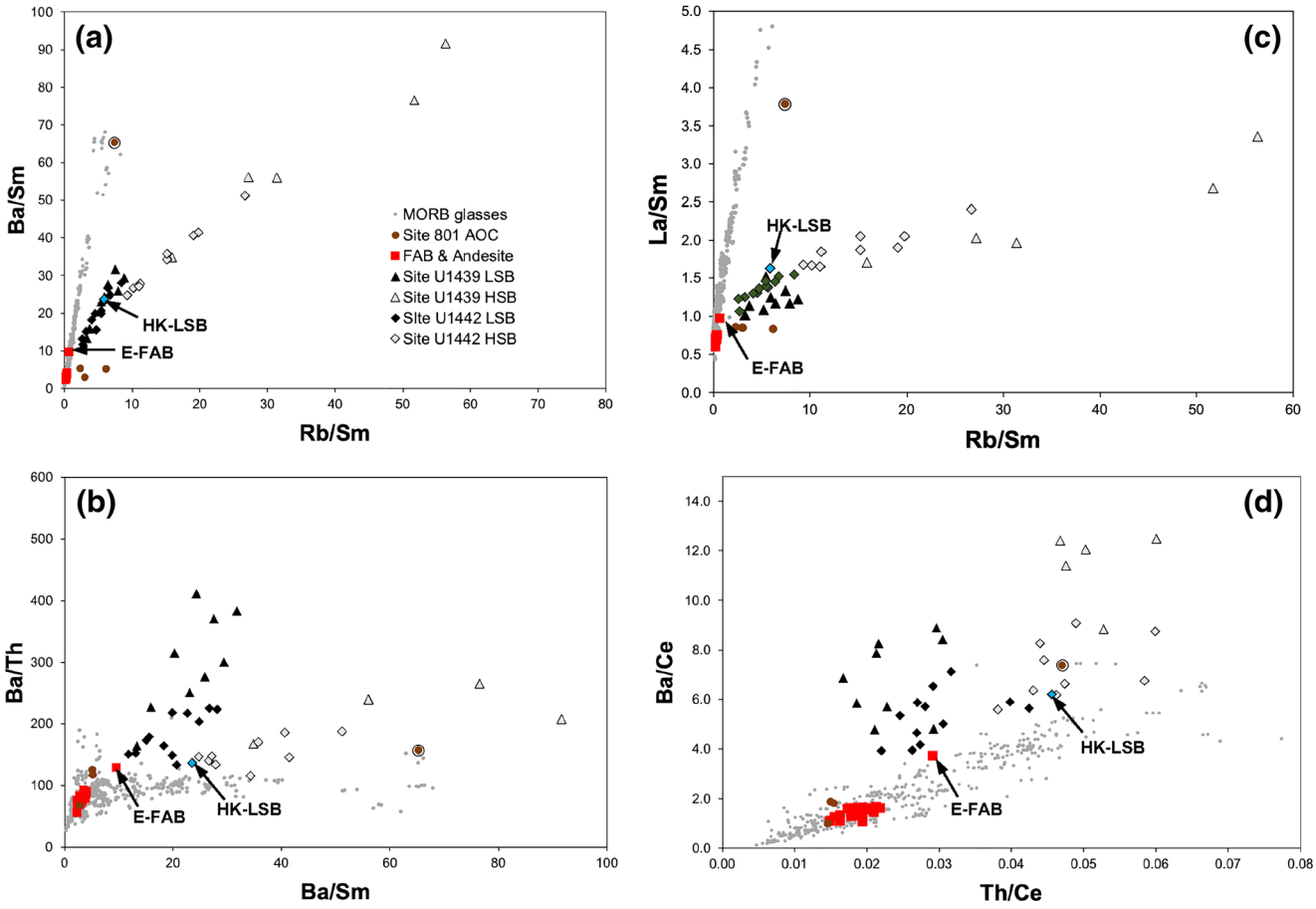


Figure 8. Incompatible trace element ratio plots for Expedition 352 glasses. MORB glass compositions (Jenner & O'Neill, 2012) and bulk composite samples of altered oceanic crust from ODP Site 801 (Kelley et al., 2003) are shown for comparison. The uppermost Site 801 composite is circled. (a) Ba/Sm versus Rb/Sm (b) Ba/Th versus Ba/Sm. (c) La/Sm versus Rb/Sm. (d) Ba/Ce versus Th/Ce. HSB, high-Si boninites; LSB, low-Si boninites; MORB, mid-ocean ridge basalt.

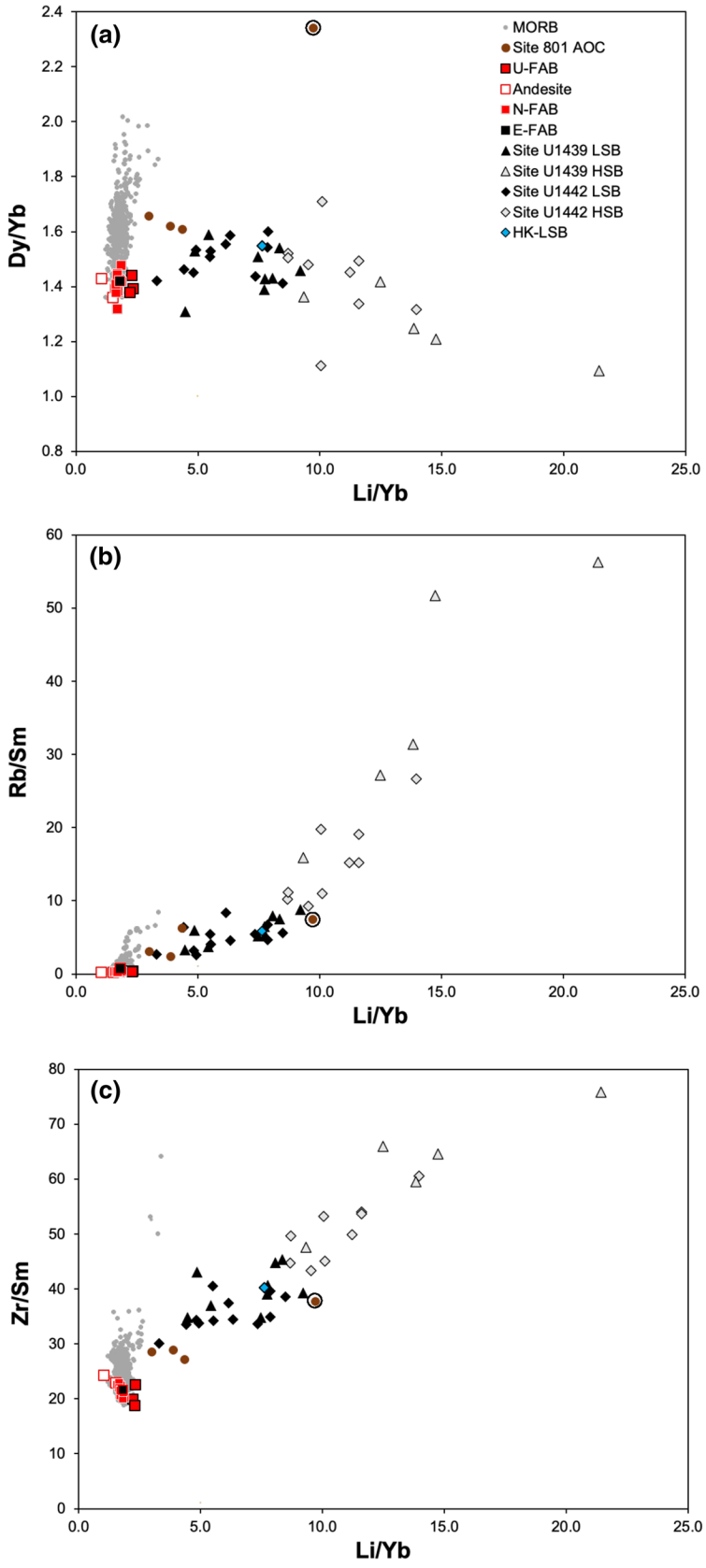
K/Ti, become more FAB-like upsection (Figure 7), whereas HSB tend to become less FAB-like upsection, especially for Hole U1439C.

V concentrations in boninite series glasses are roughly a third to a half those in FAB. However, Ti concentrations are exceedingly low in these glasses and the resulting Ti/V ratios are correspondingly low (Figure 10). This is a characteristic of boninites globally (e.g., J. W. Shervais, 1982). Cr concentrations are <360 ppm for boninite series glasses (Table S1). This contrasts with boninite whole rocks, which contain up to 1,800 ppm Cr (M. K. Reagan et al., 2017; Shervais et al., 2020).

4.3. O and H Isotopes and H_2O Concentration

Oxygen isotopes were measured on selected glasses from IODP Expedition 352 drill cores (Table S3). Replicate analyses of several samples show that glass chips collected within millimeters to centimeters of each other have variations in $\delta^{18}O$ values well above the analytical error of ±0.1‰. Average $\delta^{18}O$ values for FAB glasses range from 5.12‰ to 5.65‰, which overlap those of MORB (cf. Eiler et al., 2000a), but extend to lower values (Figure 11). Four fragments of one FAB-related andesite glass sample all have low $\delta^{18}O$ values, with a variation of 0.8 per mil (3.9‰–4.7‰). The E-FAB glass has the highest value for FAB (5.7‰).

FAB glasses have a narrow range of δD values of −67‰ to −73‰ (Figure 11), which lies within the MORB array (cf. Dixon et al., 2017). The FAB-related andesite (−61‰) and E-FAB (−55‰) have somewhat higher values. Water concentrations for the FAB reported here range from 0.29 to 0.65 wt.% (Table S3), which are


(a)
MORB
Site 801 AOC
U-FAB
Andesite
N-FAB
E-FAB
Site U1439 LSB
Site U1439 HSB
Site U1442 LSB
Site U1442 HSB
HK-LSB
Dy/Yb
Li/Yb
(b)
Rb/Sm
Li/Yb
(c)
Zr/Sm
Li/Yb

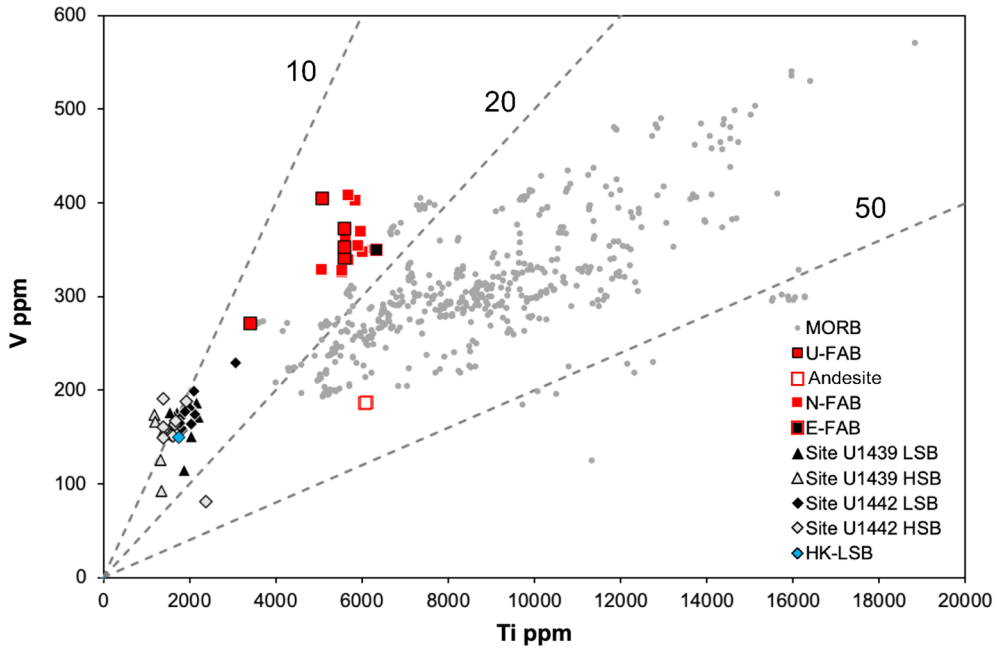


Figure 10. Plot of V versus Ti concentrations. Ti/V ratios are illustrated with dashed lines. MORB glass compositions (Jenner & O'Neill, 2012) are shown for comparison. MORB, mid-ocean ridge basalt.

similar to those of N-MORB. However, as shown above, these lavas are exceedingly depleted in incompatible trace elements, including Ce. As a result, H_2O/Ce ratios (800–1,400) are significantly higher than those of MORB (115–450: Dixon et al., 2017; Kendrick et al., 2017; le Roux et al., 2006; Loewen et al., 2019, Figure 11b). Water concentrations in the FAB-related andesite (0.75 wt.%) and E-FAB (1.76 wt.%) are higher still. The E-FAB glass had the highest H_2O/Ce of any FAB (2,800), within the range of values measured for the boninites (see below). In contrast, the FAB-related andesite has a lower H_2O/Ce ratio (484) than any FAB.

Most boninite series glasses have higher values of $\delta^{18}O$ (LSB: 5.1‰–5.8‰; HSB 5.7‰–6.2‰) than FAB but extend across the MORB array (Figure 11). All HSB series glass chips analyzed for oxygen isotopes were optically fresh, and we thus take our measured δD and $\delta^{18}O$ values for the erupted HSB series glasses to be magmatic. H_2O/Ce values for HSB series glasses range from c. 1,900 to 6,300, which should be viewed as minimum magmatic values given the abundant evidence for significant degassing of these magmas before eruption. Some LSB series glasses, however, are perlitic and their oxygen and hydrogen isotopic compositions may have been affected by low-temperature hydration. A fragment of one of these perlitic glass samples (U1442A 49R2 69/72) gave $\delta^{18}O = 5.1‰$, with a separate fragment giving $\delta^{18}O = 5.6‰$, thus implying that the oxygen isotope values for this sample were variably affected by incorporation of seawater at elevated temperatures. This alteration and modification of $\delta^{18}O$ values likely proceeded along fractures that formed due to stresses induced by cooling and hydration in a fashion similar to other subaerial pearlites (e.g., Bindeman & Lowenstern, 2016). Thus, the higher value is likely to be more representative of the magmatic value of this sample.

HSB series glasses have δD values (−62‰ to −51‰), which are higher than FAB, whereas LSB series glasses values vary more widely (−78‰ to −51‰). The LSB series glass samples with the two lowest measured δD values (−78‰ and −77‰) were likely also to have been affected by low-T hydration (see Kyser &

Figure 9. (a) Plot of Dy/Yb versus Li/Yb illustrating slightly elevated Li/Yb in the U-FAB, and differing, albeit scattered, trends for LSB series and HSB series glasses. (b) Plot of Rb/Sm versus Li/Yb showing the strong enrichments of Li and Rb in boninite series glasses, particularly HSB. (c) Plot of Zr/Sm versus Li/Yb showing that the Li and Zr enrichments in the boninites are related, and that slab fluids have higher Zr/Sm than potential sources in the subducting plate. MORB data are from Jenner and O'Neill (2012). Site 801 AOC bulk composites are from Kelley et al. (2003). The uppermost composite is circled. FAB, forearc basalts; HSB, high-Si boninites; LSB, low-Si boninites; MORB, mid-ocean ridge basalt.

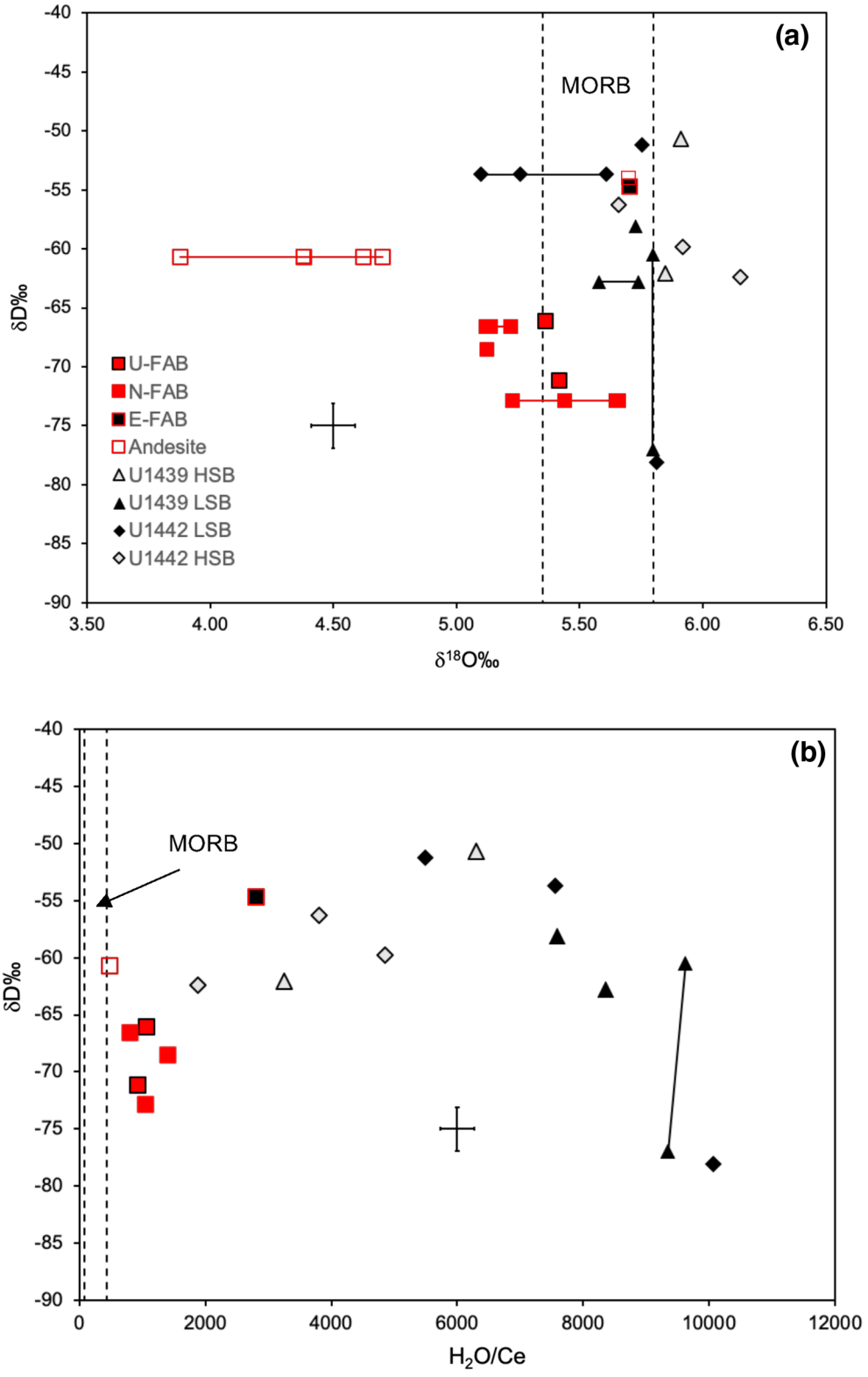


Figure 11. Stable isotope plots for glasses from IODP Expedition 352 cores. (a) Plot of δD versus $\delta^{18}O$. (b) Plot of δD versus H_2O/Ce. Values are relative to Vienna Standard Mean Ocean Water. The range for $\delta^{18}O$ in MORB is from Eiler et al. (2000b). The δD values for MORB span the entire range illustrated on the plots (Dixon et al., 2017). Representative 1σ error bars are shown. IODP, International Ocean Discovery Program; MORB, mid-ocean ridge basalt.

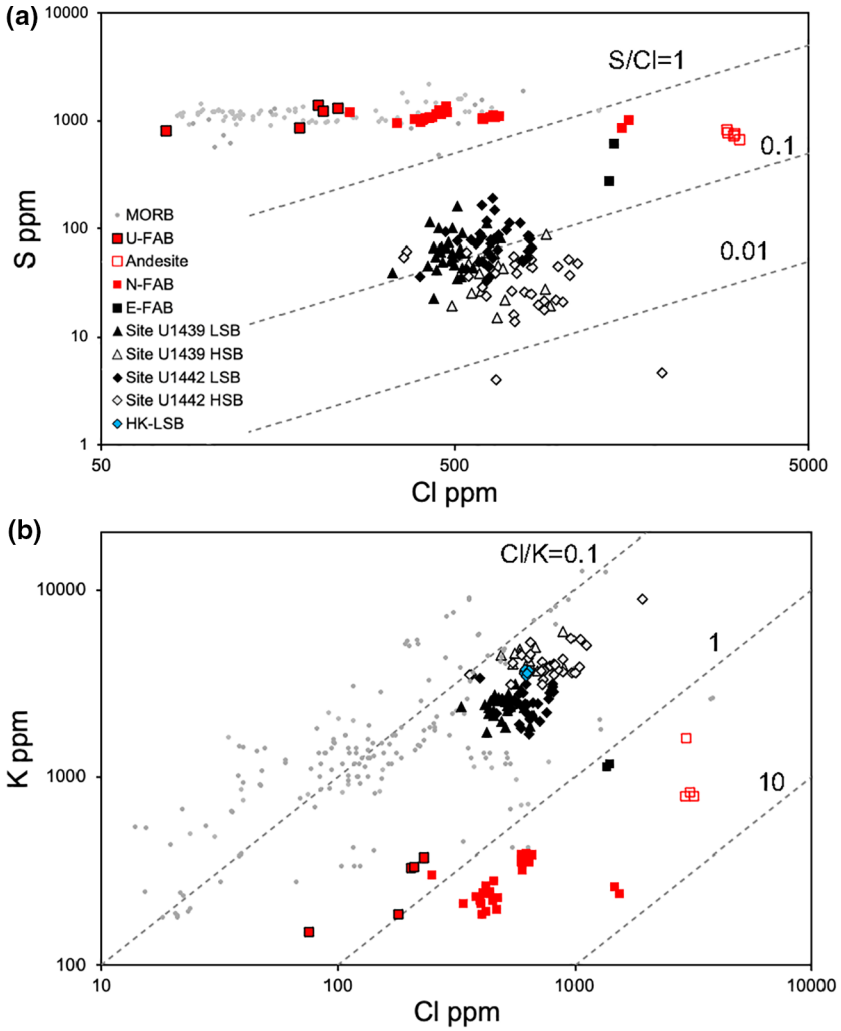


Figure 12. a) Plot of S ppm versus Cl ppm (EPMA data); (b) plot of K ppm versus Cl ppm (EPMA data) for glasses from IODP Expedition 352. Dashed lines are (a) S/Cl ratios and (b) Cl/K ratios. MORB data are from Jenner and O'Neill (2012), Kendrick et al. (2017), and Shimizu et al. (2019). EPMA, electron probe microanalyzer; IODP, International Ocean Discovery Program; MORB, mid-ocean ridge basalt.

O'Neil, 1984). One of these low δD samples has alteration minerals along fracture surfaces, and a replicate analysis of the other sample (U1442A 56R2 24/27) produced a δD value of −61‰. This raises the possibility that some of the scatter to lower δD values in boninites may also reflect secondary hydration, an interpretation which is consistent with the negative correlation of δD and H_2O/Ce on Figure 11b. We thus conclude that true magmatic $\delta^{18}O$ values for LSB lie between 5.6‰ and 5.8‰. Magmatic δD values for LSB range from −51 to perhaps as low as −63‰.

Water concentrations range from 1.32 to 1.77 wt.% in HSB series glasses, and 1.82 to 3.21 wt.% in LSB series glasses (Table S3). The highest value is for a perlitic LSB series glass (U1442A 56R2 24/27) and thus this sample likely contains secondary water.

4.4. S and Halogen Concentrations

FAB have MORB-like sulfur concentrations (Figure 12) at 800–1,400 ppm, whereas the FAB-related andesite glasses have somewhat lower concentrations (730–820 ppm) and E-FAB glasses have even lower S concentrations (275–602 ppm).

Boninite series glasses have low sulfur concentrations, typically <100 ppm and entirely <200 ppm (Table S1). Sulfur concentrations are particularly low in HSB series glasses (<63 ppm). The low S concentrations in the boninite series glasses are consistent with similarly low values observed for boninites from the nearby Bonin Islands and elsewhere (Dobson & O'Neil, 1987; Hamlyn et al., 1985), including modern LSB erupting in the northern Lau basin (e.g., Resing et al., 2011).

N-FAB glasses have Cl concentrations ranging from values typical of MORB glasses (Figure 12) up to values as high as c. 1,500 ppm. E-FAB glass has high Cl at c. 1,500 ppm, and FAB-related andesite glasses have still higher concentrations (c. 2,900 ppm; Table S1). The low concentrations of K_2O result in Cl/K values for the N-FAB that are significantly above those of most MORB (Figure 12b). U-FAB have lower Cl concentrations at 60–230 ppm.

Cl concentrations are high in both LSB and HSB series glasses (470–1,900 ppm) and tend to be higher in more differentiated glasses. Cl/K ratios are much lower in boninites compared with FAB, particularly for the HSB series glasses, reflecting their high concentrations of K. F concentrations for FAB and boninite series are similar to one another (60–190 ppm) and to MORB (Table S1). The high Cl but modest F concentrations result in low F/Cl ratios in Expedition 352 glasses (0.14–0.61) compared with those of MORB (0.3–12: see Kendrick et al., 2017; Shimizu et al., 2019).

5. Discussion

5.1. FAB

Major element compositions of FAB glasses from Sites U1440 and U1441 share many geochemical traits with highly depleted MORB, which are typically associated with shallow ridges and high potential temperatures (Gale et al., 2014; Klein & Langmuir, 1987). These traits include high FeO* and low Al_2O_3, Na_2O, TiO_2, and K_2O concentrations (Figure 4). However, SiO_2 concentrations are systematically higher (at a given MgO concentration) in FAB than MORB (Figure 4a). FAB also differ from back-arc basin basalts in that the latter typically have relatively low FeO* concentrations compared with MORB because of lower average temperatures of melting and higher average extents of melting in back-arc settings (Gale et al., 2014; Langmuir et al., 2006). The unusual combination of high SiO_2 and FeO* and low Na_2O concentrations in FAB may reflect the relatively high-T, low-P conditions of mantle melting compared with basalts produced at typical spreading centers (see Figure 14 in J. W. Shervais et al., 2019). These unusual conditions may be related to this nascent subduction setting, where near-trench seafloor spreading above a subducting slab resulted in hot mantle rising to shallow depths (Maunder et al., 2020).

FAB glasses have incompatible trace element compositions at the depleted end of the MORB array (Figure 6). Eocene basalts erupted 49–50 Ma at IODP Site 1438 (Figure 1) share these compositions, indicating that the regional asthenospheric mantle was unusually depleted at the time of subduction initiation in the IBM system (M. K. Reagan et al., 2010; J. W. Shervais et al., 2019; Yogodzinski et al., 2018). FAB glasses also have $^{87}Sr/^{86}Sr$ and $^{206}Pb/^{204}Pb$ isotopic compositions similar to those of Indian Ocean MORB and distinct from subducting Pacific MORB (H. Y. Li et al., 2019). The relatively high Ba/Sm, Th/Sm, and Nb/Sm ratios for FAB (Figure 6) may also reflect this Indian Ocean MORB-like source (e.g., Rehkämper & Hofmann, 1997).

FAB also have MORB-like S concentrations (Figure 12), so were also likely buffered by sulfide phases during melting and fractionation (e.g., Mathez, 1976). In contrast, the low concentrations of S in E-FAB series glasses probably reflect S degassing during eruption.

Some compositional traits separate FAB from MORB. For example, FAB have low Ti/V relative to MORB (Figure 10). An enrichment of V relative to Ti is expected for melts of a highly depleted mantle source (M. K. Reagan et al., 2010). However, it is also true that FAB lavas are marginally oxidized compared to average MORB (Brounce et al., 2015) and increased incompatibility during FAB genesis may have contributed to the absolute enrichment of V in FAB over MORB (see J. W. Shervais, 1982).

The chemical traits of IBM FAB were modeled in J. W. Shervais et al. (2019), who attributed FAB to 7%–23% melting of a mantle source that had undergone prior depletion hundreds of million years before subduction began (H. Y. Li et al., 2019; Yogodzinski et al., 2018).

FAB also have high H_2O/Ce and Cl/K ratios (Figures 11b and 12b) compared to all MORB (e.g., Dixon et al., 2017; Kendrick et al., 2017). The low Ce and K concentrations are a likely consequence of the extreme depletion of the mantle sources for FAB. The lack of similar depletions in H_2O and Cl may be explained if one or more of the following were true: (a) H_2O and Cl were added to the glasses by seafloor alteration (b) these chemical species were added by assimilation of crustal materials during differentiation of FAB, (c) the mantle sources for FAB were enriched in H_2O and Cl before subduction started, and/or (d) the FAB mantle sources were enriched in H_2O and Cl by subducted fluids.

Explanation (a) can be rejected because, although low-T glass hydration could raise H_2O/Ce and Cl/K ratios and lower F/Cl ratios, it also would lower rather than raise δD values because protium diffuses faster than deuterium (e.g., Kyser & O'Neil, 1984).

The combination of low $\delta^{18}O$ and δD values and F/Cl ratios in the FAB-related andesites and some differentiated N-FAB is most consistent with Explanation (b). The shift to significantly lower $\delta^{18}O$ values, while only accompanied by a minor effect on incompatible trace element patterns, is consistent with the assimilation of oceanic crust that had been hydrothermally altered at high temperature. Such shifts have been reported in doleritic to gabbroic sections from both ophiolites and oceanic crust (e.g., Cooper, 2007; Gao et al., 2012; Gregory & Taylor, 1981; Kempton et al., 1991; Michael & Schilling, 1989; Sano et al., 2008; Stakes & Taylor, 1992; Zhang et al., 2017). The low H_2O/Cl for the FAB-related andesite indicates that the assimilation may also have involved a chloride brine, as has been proposed for lavas erupted at some spreading centers (e.g., Kendrick et al., 2013).

The compositions of differentiated lavas erupted at mid-ocean ridges (e.g., Freund et al., 2013; le Roux et al., 2006; Wanless et al., 2011) and back-arc (Kent et al., 2002) settings have been explained by similar assimilation, fractional crystallization processes. However, in no case do oxygen isotopic compositions of MORB reach the low values found in FAB-related andesite glasses. We thus hypothesize that the extent of assimilation was greater in this nascent subduction setting than in other spreading center environments.

The high H_2O/Ce values in all FAB glasses compared with MORB does, however, suggest that high H_2O is an intrinsic property of parental FAB and their mantle sources. Several hypothetical scenarios can be envisioned for the presence of hydrated, but highly depleted, mantle in the IBM region in the absence of ongoing subduction (Explanation [c]), but none of them are persuasive. For example, it is possible the Philippine Sea Plate region was underlain by mantle that retained hydrogen after a history of much older subduction (see Dixon et al., 2017; Shaw et al., 2012).

FABs were generated in a supra-subduction zone environment. Thus, a simpler and more compelling argument for their relatively high Cl and H_2O concentrations is that aqueous fluids from the subducting plate were involved in their genesis (Explanation [d]). For example, adding just a few hundredths of a percent seawater or shallow pore fluids to the depleted FAB source could shift H_2O/Ce and K/Cl values to those of N-FAB while having little effect on incompatible trace element concentrations and $\delta^{18}O$ values. However, direct addition of even 0.01% seawater to FAB sources would raise δD values for the resulting mantle above those of any FAB because of the low water concentrations in depleted mantle (c. 100 ppm; Warren & Hauri, 2014). Thus, dilute subducted fluids involved in N-FAB genesis would have to have been derived from dehydration of hydrous minerals formed at relatively low temperatures (e.g., serpentine; Alt & Shanks, 2006). U-FAB's low Cl concentrations imply that any subducted fluid involved in its genesis was fresher, albeit more enriched in Li, than the one involved in N-FAB genesis (Figure 6f).

The higher incompatible trace element concentrations and flatter REE patterns in the E-FAB glass require that its parental magma was derived from a less depleted mantle source than that of other FAB, which is consistent with its relatively low Hf and Nd isotopic compositions (H. Y. Li et al., 2019). In addition, several fluid-mobile elements are enriched over REE in the E-FAB glass compared with any other lavas from Sites U1440 and U1441. (Figures 5 and 6). This glass also has H_2O concentrations, H_2O/Ce ratios, and $\delta^{18}O$ and δD values within the range of the boninite glasses (Figure 11). Considered together, these compositional traits imply that a significant flux of subducted fluid was involved in E-FAB genesis. Its low S content, high degree of differentiation, and high vesicularity provide good evidence that the E-FAB had enough water to have undergone degassing upon eruption.

Weighing all of this evidence, we conclude that FAB were generated largely by decompression melting of a highly depleted mantle immediately after subduction initiation. Subducted aqueous fluids that were dilute in terms of incompatible trace elements, but had diverse salinities, were involved in FAB genesis. For N-FAB and U-FAB, fluid involvement in melting was minimal and the resulting lavas were undersaturated in a water-rich vapor phase. In the case of E-FAB, enough fluid was added to the source to generate lavas that were saturated in water upon eruption. The fluid involved in E-FAB genesis was derived from a source that had hydrogen and oxygen isotopic compositions similar to the slab-derived materials that were involved in boninite genesis. Despite the involvement of subducted fluids in generating FAB, its Indian Ocean MORB-like radiogenic isotopic signatures were intrinsic to the mantle source (H. Y. Li et al., 2019). The trend to lower $\delta^{18}O$ and higher δD and Cl/K values in FAB-related andesites is best explained by assimilation of hydrothermally altered oceanic crust during differentiation.

5.2. Boninite Series

5.2.1. Differentiation

The primary focus of this paper is on the implications of glass compositions for the nature of mass transfer from the subducting plate during magma genesis after subduction initiation. Nevertheless, boninite glass compositions are relatively fractionated and classify as HMA (Figure 3). Thus, the nature of this fractionation merits some discussion. Important in this discussion is the observation that boninite whole rocks are highly porphyritic and have MgO concentrations as high as 18 wt.% (Shervais et al., 2020.). Because FeO* concentrations are relatively low in boninites recovered during Expedition 352, primary compositions for these boninites have c. 12–13 wt.% MgO and FeO*/MgO = 0.56 – 0.68 to be in equilibrium with the most forsteritic olivine crystals found in the boninites (Fo_{92}; Whattam et al., 2020). Boninites with higher MgO concentrations than this, which is about two thirds of samples, have accumulated crystals (Shervais et al., 2020).

The suites of LSB series glasses from the two sites produce parallel calc-alkaline trends, with glasses from Site U1442 having higher FeO*/MgO (Figure 13a) ratios but lower SiO_2 and MgO concentrations compared with Site U1439 glasses (Figure 4). This suggests that primitive magmas lavas were less silicious and that differentiation was more extensive at Site U1442 compared with Site U1439. The least differentiated glasses at both sites are offset to higher FeO*/MgO ratios and SiO_2 concentrations compared with primitive boninite compositions (Shervais et al., 2020, Figure 13b), and the increase in FeO*/MgO ratios with increasing SiO_2 concentrations for all but the most silicic series glasses (Figure 13a) is less than predicted by the crystal fractionation modeling program COMAGMAT (Almeev et al., 2007, 2012; Ariskin, 1999). The increase on FeO* over MgO in the models reflects clinopyroxene followed by clinopyroxene + plagioclase fractionation (Figure 13a).

HSB series glasses for the two sites have overlapping compositions, and thus, are discussed together. Like LSB series glasses, HSB series glasses plot at higher FeO*/MgO values than for primitive HSB compositions (Shervais et al., 2020, Figure 13). The trends for differentiated HSB series glasses also do not follow modeled crystal fractionation trends. Instead, as concentrations of SiO_2 increase, FeO*/MgO values first rise less than predicted by crystal fraction models, then rise more steeply, producing an overall trend of an increasing rate of FeO*/MgO rise with increasing SiO_2. This trend may be explained by mixing between less fractionated and more fractionated HSB melt compositions (Figure 13). The few highly differentiated LSB series glasses that were analyzed plot along a similar trend of progressively greater enrichment in FeO*/MgO with increasing SiO_2 concentrations.

Our working hypothesis to explain the twin observations that most boninite whole rocks have compositions affected by crystal accumulation and glasses have compositions consistent with mixing between less and more fractionated liquids (Figure 13b) is that most eruptions involve intrusion of relatively undifferentiated magmas into crystal mushes that consists of accumulated crystals with interstitial melt (e.g., Bergantz et al., 2015). The resulting melt mixtures as recorded in the glasses have compositions lying along trends between interstitial melts in the mush and the intruding magma (e.g., Lissenberg et al., 2019), whereas whole boninitic lavas have compositions lying between the intruding magma compositions and the mushes with accumulated crystals (Figure 13b).

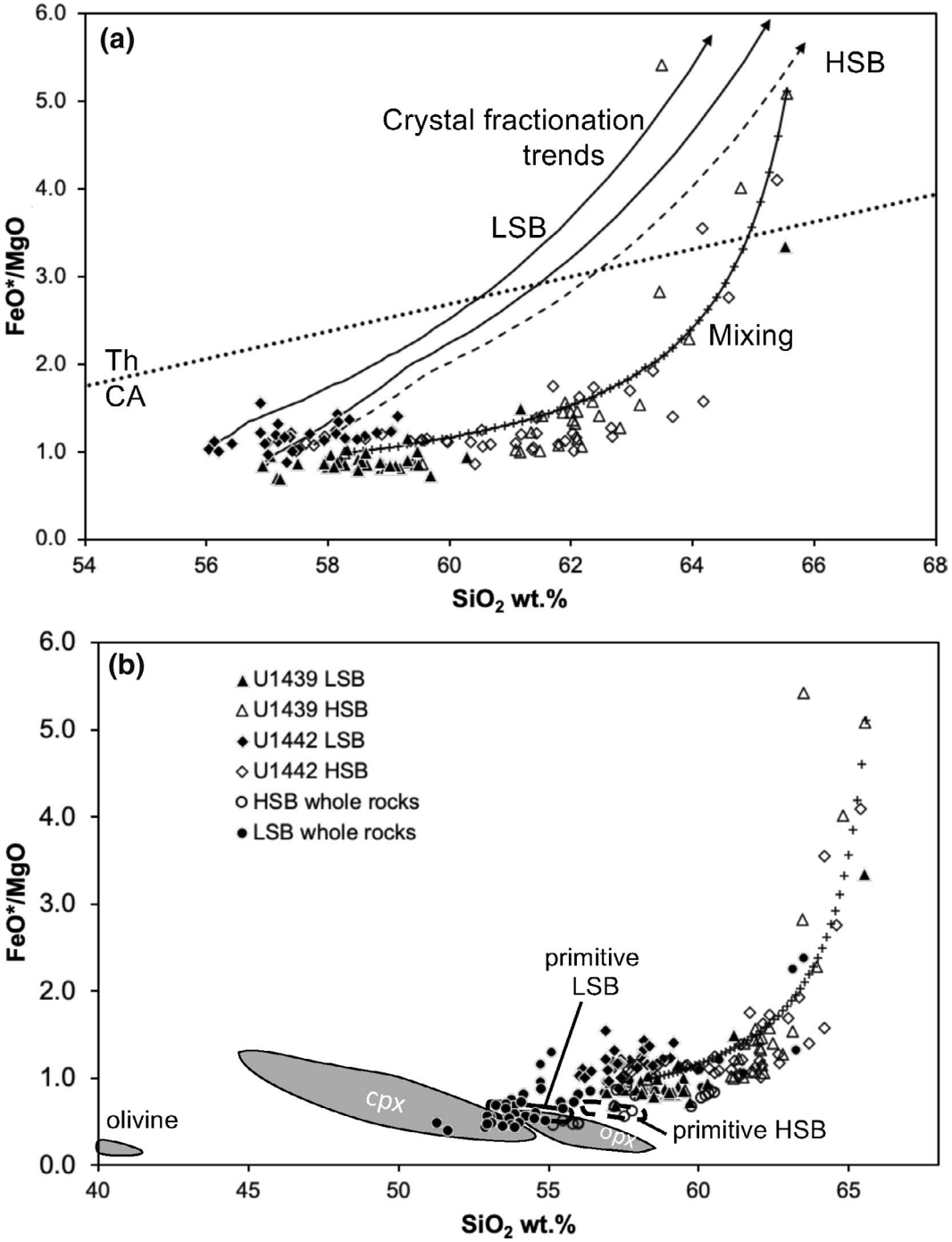


Figure 13. Plots of total iron as FeO over MgO (FeO*/MgO) versus concentrations of SiO_2. (a) Glass compositions and modeling. The dotted line is the boundary used to separate calc-alkaline (CA) and tholeiitic (Th) magma series from Miyashiro (1974). Arrows show crystal fractionation trends produced by COMAGMAT ver. 3.72 (Ariskin, 1999; Almeev et al., 2007, 2012). Solid arrows are for LSB (glasses U1439C 36R-1 64/66; U1442A 30R-4 45/47); the dashed arrow is for HSB (glass U1442A 15R-1 0/2). All assume 3 kbars of pressure and 2 wt% water. Varying these parameters changes the precise fractionation trends, but all trends using water concentrations ranging from 1 to 4 wt% and 1–3 kbars (not shown) are steeper than the general orientation of the fields for boninite glasses. Mixing between a more and a less primitive HSB glass composition also is shown, with plus symbols representing 2% mixing steps. (b) Plot with expanded SiO_2 concentrations showing compositions of mafic minerals from Whattam et al. (2020) and boninite whole-rock compositions from Shervais et al. (2020). Approximate fields for primitive melt compositions based on equilibrium with Fo 91–92 compositions are illustrated in solid (LSB) and dashed (HSB) outlines. Note the significant number of whole-rock compositions that imply crystal accumulation. HSB, high-Si boninites; LSB, low-Si boninites.

5.2.2. Magma Sources and Melting

For primary LSB lavas to plot in their namesake field on Figure 3, the extents of source depletion and degrees of melting must have been high enough for melting to extend beyond clinopyroxene exhaustion (J. A. Pearce & Reagan, 2019). Similarly, the high SiO_2 and low CaO concentrations of HSB parental magmas require shallow melting of mantle with minimal clinopyroxene, such that the primary magma was generated mostly by incongruent melting of orthopyroxene (Shervais et al., 2020). Melting of refractory mantle requires the presence of significant water at the potential temperatures possible in this modern earth, subduction initiation environment (J. A. Pearce & Reagan, 2019).

This progressive depletion of mantle through time is reflected in progressively lower middle and heavy REE concentrations in FAB through LSB series to HSB series glasses, and is the likely result of continual melting and remelting of asthenospheric mantle trapped above the new subducting plate. During this period of "trapped" asthenosphere, magma genesis likely changed progressively from predominantly decompression melting (to generate FAB), through a transitional stage (to generate LSB) to predominantly water-assisted melting of the residue after FAB and LSB genesis (to generate HSB), all without significant replenishment of the mantle by convection (M. K. Reagan et al., 2017; Shervais et al., 2020). These changes in concentration in the studied glasses are accompanied by changes in REE patterns from light REE-depleted in FAB, through weakly light REE-depleted to nearly flat in LSB series glasses, to U-shaped in HSB series glasses (Figure 5).

Enrichments in fluid-mobile elements (including Zr) for decreasing middle REE concentrations characterizes both LSB and HSB (Figure 5) and has been attributed to progressive flux melting involving water-rich melts that were derived, at least in part, from subducted amphibolitic crust (H. Y. Li et al., 2019). The implied temperatures in slab crust at the slab-mantle interface are therefore high relative to those in normal subduction zones (see Maunder et al., 2020). The separate trace element (Shervais et al., 2020) and isotopic trends (H. Y. Li et al., 2019) for LSB and HSB illustrate that the compositions of slab melts involved in their genesis differed for these two magma suites. Isotopic fingerprinting provided evidence that the slab melts involved in LSB genesis were essentially restricted to subducted Pacific basaltic crust, whereas sediments were additionally involved in HSB genesis (H. Y. Li et al., 2019). H_2O concentrations in all pristine boninite series glasses from the drill cores are relatively high, and in the range reported for glasses from Bonin Ridge islands (e.g., Dobson & O'Neil, 1987; Umino et al., 2015). All boninites also provide abundant physical evidence for water degassing before eruption, including high vesicularity and crystallinity, as well as the common presence of hyaloclastites in drill cores (M. K. Reagan et al., 2015). Thus, the H_2O concentrations of boninite series glasses (and the E-FAB discussed above) reflect some degree of degassing prior to and during eruption on the ocean floor as well as providing evidence that all slab melts involved in boninite genesis were water-rich. This degassing likely caused magmas also to lose S, although the low S concentrations in boninites may also reflect strong prior depletion of the mantle source (Valetich et al., 2019).

Ratios between more and less fluid-mobile elements for LSB and HSB series glasses are used here to further identify sources for their parental magmas (Figures 8 and 9). LSB series glasses form linear trends on some bivariate plots involving ratios between variously fluid-mobile elements, but form fields on other plots. For example, the plot of Ba/Sm against Rb/Sm (Figure 8a) shows that the slab fluids involved in LSB genesis must have had essentially unchanging Ba/Rb ratios. In contrast, LSB series glasses form fields with quasiapexes of FAB, HK-LSB (with low Ba/Th) and magmas with high Ba/Th (Figures 8b and 8d), showing that compositionally variable subducted components were involved in LSB genesis. The trends and fields for LSB series glasses on these plots approach the MORB-FAB array. There is abundant textural evidence for magma mixing and mingling in boninite cores from Expedition 352 (M. K. Reagan et al., 2015), so these trends may be the result of mixing between simultaneously generated boninite and FAB. However, the trends toward FAB-like compositions also may reflect variable source depletion (H. Y. Li et al., 2019) or FAB retention in pores or veins by the mantle sources for boninites (Shervais et al., 2020).

Most incompatible trace element ratios in LSB series glasses lie within the field of ratios plotted for altered basaltic crust composites from ODP Site 801 in the western Pacific (see Kelley et al., 2003), which is consistent with isotopic evidence that the slab constituents in LSB were derived from altered oceanic crust (H. Y. Li et al., 2019). More specifically, the source of the subduction component in those LSB with lower La/Sm

ratios resembles altered normal MORB crust, though with enhanced concentrations of some incompatible elements such as Ba. In contrast, the HK-LSB end-member often plots between altered normal MORB and the more alkaline altered lavas that cap the Site 801 crustal section (those circled on Figure 8).

Plots of Dy/Yb against Li/Yb (Figure 9a) are particularly useful in constraining the sources of slab fluids (e.g., J. G. Ryan & Langmuir, 1987). Li/Yb ratios are high in LSB series lavas and they correlate with other trace element ratios that are associated with flux melting (e.g., Rb/Sm, Figure 9b), thus confirming the mobility of Li during subduction (see J. G. Ryan & Langmuir, 1987). Dy/Yb ratios are generally higher in LSB series glasses than in FAB glasses but overlap those in Site 801 altered oceanic crust (Kelley et al., 2003). The high Zr/Sm ratios for LSB series glasses (Figure 9c) support models in which LSB genesis involved melts of the subducted altered oceanic crust with an amphibole-bearing residue (H. Y. Li et al., 2019). Amphibole/melt partition coefficients are in the order: $D_{Dy} > D_{Yb} > D_{Li}$ (J. G. Ryan & Langmuir, 1987), so an additional phase must have been important for maintaining low D_{Zr}/D_{Sm} while raising the bulk D_{Yb}/D_{Dy} in the residue left from the melting episode that generated LSB. A small proportion of garnet, or a significant proportion of clinopyroxene in the residue, would have this effect (see Gaetani et al., 2003).

Thermomechanical modeling of the initiation of subduction in Maunder et al. (2020) shows temperatures rising above the solidus for the hottest subducted altered oceanic crust about 500 Kyr after subduction initiation. Such a timescale is on the same order as the time interval between earliest FAB volcanism and the onset of LSB volcanism (cf. M. K. Reagan et al., 2019). These supra-solidus conditions occur at exceedingly shallow levels beneath the proto-forearc 0.2–0.5 GPa (Figure 13), which is consistent with P-T conditions needed to generate Expedition 352 LSB (Shervais et al., 2020; Whattam et al., 2020). This extreme heating may have resulted from the rapid convection of hot asthenospheric mantle around the leading edge of the subducting crust.

Phase equilibria modeling illustrated in Figure 14 employed THERMOCALC and the methodologies of Powell and Holland (1988) and Holland and Powell (2011). Figures 14a and 14c show the results for the composite altered MORB from ODP Site 801 (Kelley et al., 2003) along the P-T path of the hottest subducting basaltic crust from the Maunder et al. (2020) model. The subducting crust crosses the solidus at c. 0.2 GPa and 700°C and melts rapidly then more slowly with continued subduction. The resulting melt is rhyolitic, leaving a residue that has roughly equal proportions of hornblende and clinopyroxene, with lesser plagioclase and minor Fe-Ti oxides (Figure 14; Table S4). This residual assemblage is consistent with trace element compositions discussed above for Expedition 352 LSB (see also Shervais et al., 2020).

HSB series glasses trend away from the HK-LSB glass composition and toward extreme incompatible trace element ratios, (e.g., Rb/Sm, Zr/Sm, Li/Yb: Figures 8 and 9). Thus, genesis of HSB involved water-rich slab melts derived from sources like those involved in generating HK-LSB and those with greater enrichments in Rb over Ba and Ba over Th. The very low concentrations of REE (particularly middle REE), combined with high Zr/Sm ratios, imply that the slab melt source had amphibole, and perhaps accessory phases such as apatite and titanite, remaining in the residue after melting (see J. A. Pearce et al., 1992; Prowatke & Klemme, 2006; Tiepolo et al., 2002). The trend to high Li/Yb, but low Dy/Yb ratios, in the HSB series glasses implies that $D_{Dy} > D_{Yb} > D_{Li}$ when the slab melt involved in HSB genesis was produced, which further implies that the sedimentary source for this slab melt was garnet-free.

The thermomechanical model of Maunder et al. (2020) and the isotopic compositions of the boninites (H. Y. Li et al., 2019) both require that sediments lagged behind subduction of basaltic crust and heated more slowly, with first melting of subducted sediment beginning at c. 800 Kyr after subduction initiation (Figure 14b). In the phase equilibria modeling of ODP Site 800 materials (Plank & Langmuir, 1998), pelagic sediment began to melt at a greater depth than that for initiation of melting of the basaltic crust (c. 0.7 GPa). This melt also is rhyolitic (Table S5) leaving a residue containing significant hornblende and minor titanite (Figure 13d). This residual assemblage also has significant biotite, which would have the effect of raising D_{Li} with respect to D_{Yb}, so the sediment involved in HSB genesis may have been less potassic than the one that was modeled. Garnet joins this assemblage at ~1 GPa, so the sediment melting would have to have been confined to pressures less than this.

Cl concentrations in all boninite series glasses are similar to, or marginally higher than, those of FAB, but Cl/K ratios are much lower (Figure 12). This is particularly true for HSB series glasses, because of their high K_2O concentrations. K is a fluid-mobile element, and its enrichment in boninites is a result of its

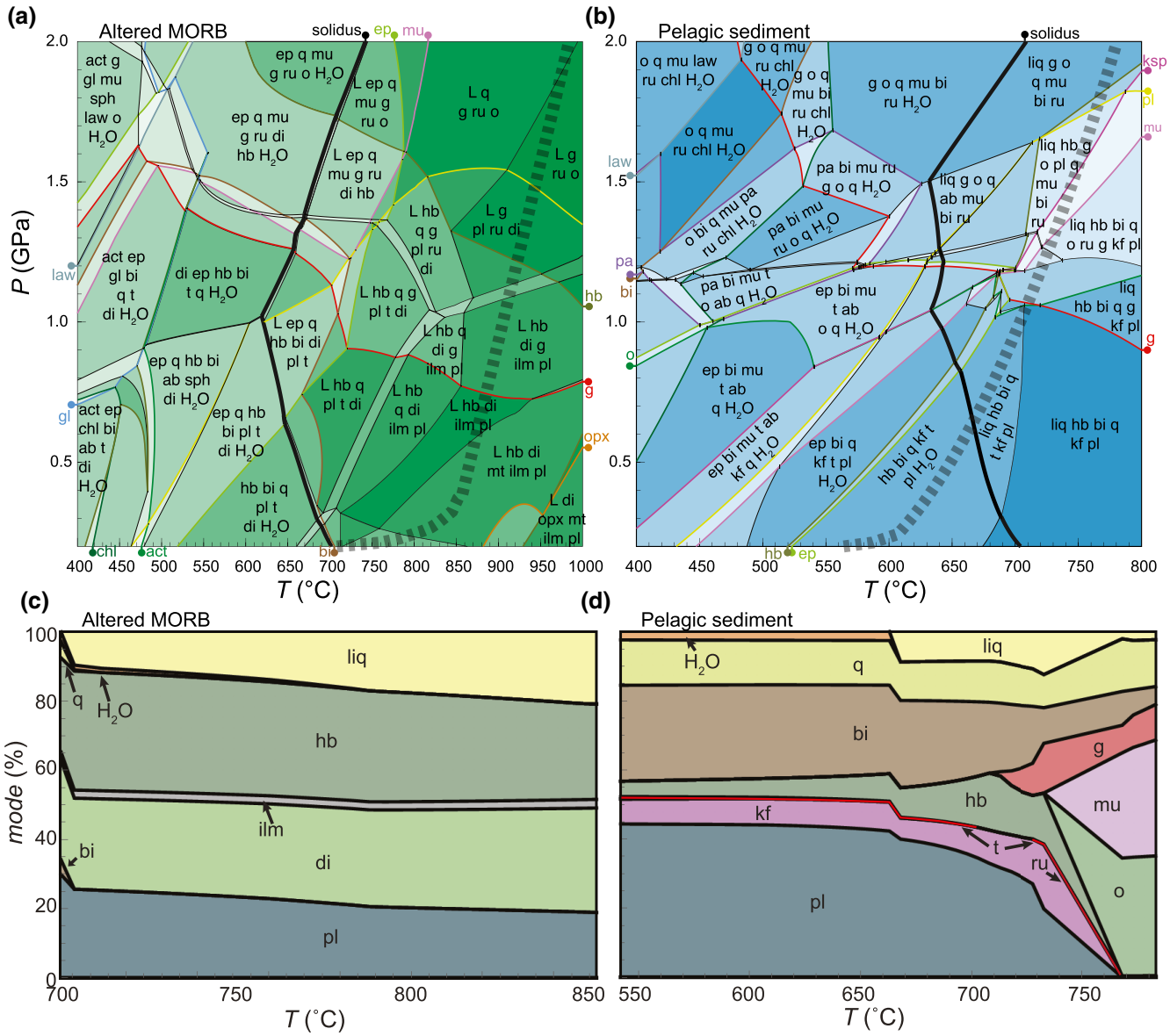


Figure 14. Phase equilibria modeling for subducted sources for IBM boninites. Modeling was performed in the NCKFMASHTO chemical system (Na_2O–CaO–K_2O–FeO–MgO–Al_2O_3–SiO_2–H_2O–TiO_2–O) using THERMOCALC version 3.45i (Powell & Holland, 1988) and the internally consistent thermodynamic dataset 6.2 (updated February 6, 2012: Holland & Powell, 2011). (a) Pseudosection for altered MORB based on ODP site 801 composite altered mid-ocean ridge basalt after Kelley et al. (2003). (b) Pseudosection for pelagic sediment from ODP site 800 after Plank and Langmuir (1998). The thick dashed lines in (a) and (b) are the P-T paths for the hottest basaltic crust and sediment respectively after subduction initiation from Maunder et al. (2020). (c) and (d) modes for phases along the P-T paths in (a) and (b), respectively. Redox conditions were fixed at $Fe^{3+}/(Fe^{3+} + Fe^{2+}) = 0.15$ for the altered basalt and 0.05 for pelagic sediment. Fluid was fixed to just saturate the assemblages at the solidus at high-pressure. Mineral activity-composition models and abbreviations include: glaucophane (gl), actinolite (act), hornblende (hb), omphacite (o), diopside (di), tonalite melt (L: Green et al., 2016), plagioclase (pl) and K-feldspar (kf) Holland & Powell, 2003), garnet (g), paragonite (pa), biotite (bi), muscovite (mu), chlorite (chl), haplogranitic melt (liq: White et al., 2014), ilmenite (ilm), magnetite (mt: White et al., 2000), orthopyroxene (opx), epidote (ep: Holland & Powell, 2011). Phases treated as pure include lawsonite (law), albite (ab), rutile (ru), titanite (t), quartz (q), and H_2O. IBM, Izu-Bonin-Mariana; MORB, mid-ocean ridge basalt.

enrichment in the water-rich slab melt that fluxed the melting region. This slab melt, therefore, must have relatively low Cl/K ratios, consistent with derivation by dehydration and melting of subducted materials as modeled above. The higher primary $\delta^{18}O$ (5.6‰–6.2‰) and δD values (−63‰ to −51‰) of boninites compared with most FAB (Figure 11) indicates that the slab melts were derived from both the altered basalt and sedimentary sections of the subducting oceanic crust, which had high values for these parameters

compared with the ambient mantle. This in turn implies that these slab melts were likely derived from the upper layers of subducting crust (e.g., Dobson & O'Neil, 1987; Eiler et al., 2000b). Other potential causes, such as low-T hydration of the glasses, assimilation of high-T altered crust by magmas, or direct addition of seawater to magmas are less likely as they would result in opposite shifts in $\delta^{18}O$ and δD values or lowering of both values (e.g., degassing of water; see Kyser & O'Neil, 1984).

Taken as a whole, it is clear that that all boninites were produced to a significant extent by flux melting of mantle sources that were depleted by prior FAB genesis. Flux melting was caused by the invasion of this highly depleted mantle by water-rich melts from the newly subducting Pacific plate. Glass data support isotope-based interpretations that the slab melts involved in LSB genesis were largely derived from subducted altered basaltic crust, whereas melts derived both from subducted sediment and altered basaltic crust are required to explain the genesis of HSB. LSB generation involved both high- and low-Ba/Th slab melts derived from altered MORB, as well as potential inmixing of FAB. This means that decompression melting likely continued after flux melting began, that is that LSB erupted during a final stage of spreading of the ocean basin in which the FAB were erupted. HSB genesis by flux melting involved that same lower Ba/Th slab melt (HK-LSB), as well as water-rich melts of sediment. All of this melting to generate boninite took place at exceedingly shallow pressures above the newly subducting Pacific plate.

6. Conclusions

1. The IBM forearc consists of lithosphere produced in the immediate aftermath of the initiation of Pacific plate subduction. IODP Expedition 352 drilled this lithosphere, recovering abundant pristine volcanic glasses, the chemical compositions of which are reported here.
2. These compositions indicate that first seafloor spreading after subduction initiation produced basalts generated by decompression melting during slab rollback of an unusually depleted mantle source. Initial melting involved a minor flux of dilute aqueous fluids perhaps derived from the dehydration of serpentine. Rare enriched E-FAB lavas interbedded with N-FAB deep in Hole U1440B, have modest enrichments in some fluid-mobile elements, are rich in water and have higher O and H isotope compositions than N-FAB, and thus were likely generated in the presence of less dilute fluids derived from dehydration of the newly subducting plate.
3. Low oxygen isotope values for FAB-related andesites indicate that these early lavas assimilated hydrothermally altered doleritic or gabbroic crust as they differentiated.
4. LSB were generated while seafloor spreading continued and were sourced in mantle that previously had melted to generate FAB. Melting took place in the presence of two end-member water-rich melts derived from subducting altered basaltic crust. One end-member had incompatible trace element compositions similar to those of typical altered normal MORB with enrichments in fluid-mobile elements, particularly Ba. The other had a composition more akin to enriched basalt, but one that was less prominently enriched in Ba. LSB also may have mixed with FAB, illustrating that magmas generated by decompression melting and by flux melting may have been generated simultaneously.
5. HSB were generated from strongly depleted mantle after seafloor spreading had largely ceased. Magma generation involved the same low-Ba slab melt involved in LSB genesis plus another derived by dehydration and melting of subducting Pacific sediments.
6. Thermodynamic modeling provides evidence that the slab melts responsible for mantle melting and boninite genesis were derived from subducted altered oceanic crust at 0.2–0.5 GPa (to form LSB) and altered oceanic crust plus sediment at 0.6–1 GPa (to form HSB).
7. We interpret the progressive depletion of the FAB to LSB to HSB series glasses to be the result of progressive melting of asthenospheric mantle without significant refertilization or replenishment. The switchover to arc volcanism with more typical SiO_2-TiO_2-MgO systematics at c. 44 Ma (e.g., Ishizuka et al., 2006, 2011; M. K. Reagan et al., 2008) likely marked the beginning of mantle counterflow. Thus, the asthenosphere apparently was trapped within the mantle wedge and progressively melted over the first c. 7–8 Myr after subduction initiation and before mantle counterflow became vigorous enough to enable fertile mantle to penetrate the proto-mantle wedge and so begin to generate nonboninitic arc magmas.

8. Glass compositions for boninites can be explained by mixing between the interstitial melts of relatively undifferentiated magmas with the evolved interstitial melts within crystal mushes.

Data Availability Statement

Data in Tables S1-S3 may be found in Coulthard et al. (2020; https://doi.org/10.26022/IEDA/111722).

Acknowledgments
This research used samples and data provided by the International Ocean Discovery Program (IODP). We thank the crew of the JOIDES Resolution, the science team, and the technical support staff for IODP Expedition 352 for making this research possible. We particularly thank staff scientist Katerina Petronotis for her guidance throughout the expedition. Ben Maunder provided P-T paths for subducted materials. Postexpedition awards from the US Science Support Program to Reagan, Shervais, and Ryan, and US-NSF grants OCE1558647 (Reagan). OCE1558689 (Shervais) and OCE1558855 (Ryan) supported this research. Almeev was supported by the German Science Foundation (DFG Project AL1189/8-1). Brounce acknowledges support from the University of California Riverside. Pearce thanks the NERC (UK) for grant NE/M012034/1. Chapman was supported by the Australia-New Zealand IODP consortium and the ARC LIEF scheme (LE140100047). This paper benefitted significantly from reviews by Karsten Haase, Heather Handley, Michael Perfit, and Kaj Hoernle.

References

Almeev, R. R., Holtz, F., Koepke, J., & Parat, F. (2012). Experimental calibration of the effect of H_2O on plagioclase crystallization in basaltic melt at 200 MPa. *American Mineralogist*, *97*(7), 1234–1240. https://doi.org/10.2138/am.2012.4100

Almeev, R. R., Holtz, F., Koepke, J., Parat, F., & Botcharnikov, R. E. (2007). The effect of H_2O on olivine crystallization in MORB: Experimental calibration at 200 MPa. *American Mineralogist*, *92*(4), 670–674. https://doi.org/10.2138/am.2007.2484

Alt, J. C., & Shanks, W. C., III (2006). Stable isotope compositions of serpentinite seamounts in the Mariana forearc: Serpentinization processes, fluid sources and sulfur metasomatism. *Earth and Planetary Science Letters*, *242*(3–4), 272–285. https://doi.org/10.1016/j.epsl.2005.11.063

Ariskin, A. A. (1999). Phase equilibria modeling in igneous petrology: Use of COMAGMAT model for simulating fractionation of ferro-basaltic magmas and the genesis of high-alumina basalt. *Journal of Volcanology and Geothermal Research*, *90*, 115–162. https://doi.org/10.1016/S0377-0273(99)00022-0

Bergantz, G. W., Schleicher, J. M., & Burgisser, A. (2015). Open-system dynamics and mixing in magma mushes. *Nature Geoscience*, *8*(10), 793–796. https://doi.org/10.1038/ngeo2534

Bindeman, I. N., Kamenetsky, V., Palandri, J., & Vennemann, T. (2012). Hydrogen and oxygen isotope behavior during variable degrees of upper mantle melting: Example from the basaltic glasses from Macquarie Island. *Chemical Geology*, *310–311*, 126–136. https://doi.org/10.1016/j.chemgeo.2012.03.031

Bindeman, I. N., & Lowenstern, J. B. (2016). Low-δD hydration rinds in Yellowstone perlites record rapid syneruptive hydration during glacial and interglacial conditions. *Contributions to Mineralogy and Petrology*, *171*, 89. https://doi.org/10.1007/s00410-016-1293-1

Brounce, M., Kelley, K. A., Cottrell, E., & Reagan, M. K. (2015). Temporal evolution of mantle wedge oxygen fugacity during subduction initiation. *Geology*, *43*(9), 775–778. https://doi.org/10.1130/G36742.1

Cooper, K. M. (2007). Data report: Trace element analyses in whole-rock basement samples, site 1256, ODP Leg 206. In D. A. H. Teagle, D. S. Wilson, G. A. Acton, & D. A. Vanko (Eds.), *Proceedings of the Ocean Drilling Program - Scientific Results* (Vol 206, pp. 1–10). College Station, TX: Ocean Drilling Program. https://doi.org/10.2973/odp.proc.sr.206.010.2007

Crawford, A. J., Falloon, T. J., & Green, D. H. (1989). Classification, petrogenesis and tectonic setting of boninites. In A. J. Crawford (Ed.), *Boninites: And related rocks* (pp. 1–49). London, UK: Unwin and Hyman.

DeBari, S. M., Taylor, B., Spencer, K., & Fujioka, K. (1999). A trapped Philippine Sea plate origin for MORB from the inner slope of the Izu–Bonin Trench. *Earth and Planetary Science Letters*, *174*(1), 183–197. https://doi.org/10.1016/S0012-821X(99)00252-6

Deschamps, A., Monié, P., Lallemand, S., Hsu, S. K., & Yeh, K. Y. (2000). Evidence for Early Cretaceous oceanic crust trapped in the Philippine Sea Plate. *Earth and Planetary Science Letters*, *179*(3), 503–516. https://doi.org/10.1016/S0012-821X(00)00136-9

Dilek, Y., & Furnes, H. (2009). Structure and geochemistry of Tethyan ophiolites and their petrogenesis in subduction rollback systems. *Lithos*, *113*(1–2), 1–20. https://doi.org/10.1016/j.lithos.2009.04.022

Dixon, J. E., Bindeman, I. N., Kingsley, R. H., Simons, K. K., Le Roux, P. J., Hajewski, T. R., et al. (2017). Light stable isotopic compositions of enriched mantle sources: Resolving the dehydration paradox. *Geochemistry, Geophysics, Geosystems*, *18*(11), 3801–3839. https://doi.org/10.1002/2016GC006743

Dobson, P. F., Blank, J. G., Maruyama, S., & Liou, J. G. (2006). Petrology and geochemistry of boninite-series volcanic rocks, Chichi-Jima, Bonin islands, Japan. *International Geology Review*, *48*(8), 669–701.

Dobson, P. F., & O'Neil, J. R. (1987). Stable isotope compositions and water contents of boninite series volcanic rocks from Chichi-jima, Bonin islands, Japan. *Earth and Planetary Science Letters*, *82*(1–2), 75–86. https://doi.org/10.1016/0012-821X(87)90108-7

Eiler, J. M., Crawford, A., Elliott, T., Farley, K. A., Valley, J. W., & Stolper, E. M. (2000b). Oxygen isotope geochemistry of oceanic-arc lavas. *Journal of Petrology*, *41*(2), 229–256.

Eiler, J. M., Schiano, P., Kitchen, N., & Stolper, E. M. (2000a). Oxygen-isotope evidence for recycled crust in the sources of mid-ocean-ridge basalts. *Nature*, *403*(6769), 530–534.

Freund, S., Beier, C., Krumm, S., & Haase, K. M. (2013). Oxygen isotope evidence for the formation of andesitic-dacitic magmas from the fast-spreading Pacific–Antarctic Rise by assimilation-fractional crystallisation. *Chemical Geology*, *347*, 271–283. https://doi.org/10.1016/j.chemgeo.2013.04.013

Gaetani, G. A., Kent, A. J., Grove, T. L., Hutcheon, I. D., & Stolper, E. M. (2003). Mineral/melt partitioning of trace elements during hydrous peridotite partial melting. *Contributions to Mineralogy and Petrology*, *145*(4), 391–405. https://doi.org/10.1007/s00410-003-0447-0

Gale, A., Dalton, C. A., Langmuir, C. H., Su, Y., & Schilling, J. G. (2013). The mean composition of ocean ridge basalts. *Geochemistry, Geophysics, Geosystems*, *14*(3), 489–518. https://doi.org/10.1029/2012GC004334

Gale, A., Langmuir, C. H., & Dalton, C. A. (2014). The global systematics of ocean ridge basalts and their origin. *Journal of Petrology*, *55*(6), 1051–1082. https://doi.org/10.1093/petrology/egu017

Gao, Y., Vils, F., Cooper, K. M., Banerjee, N., Harris, M., Hoefs, J., et al. (2012). Downhole variation of lithium and oxygen isotopic compositions of oceanic crust at East Pacific Rise, ODP Site 1256. *Geochemistry, Geophysics, Geosystems*, *13*(10), Q10001. https://doi.org/10.1029/2012GC004207

Godard, M., Dautria, J. M., & Perrin, M. (2003). Geochemical variability of the Oman ophiolite lavas: Relationship with spatial distribution and paleomagnetic directions. *Geochemistry, Geophysics, Geosystems*, *4*(6), 8609. https://doi.org/10.1029/2002GC000452

Green, E. C. R., White, R. W., Diener, J. F. A., Powell, R., Holland, T. B. J., & Palin, R. M. (2016). Activity–composition relations for the calculations of partial melting equilibria for metabasic rocks. *Journal of Metamorphic Geology*, *34*, 845–869.

Gregory, R. T., & Taylor, H. P., Jr. (1981). An oxygen isotope profile in a section of Cretaceous oceanic crust, Samail Ophiolite, Oman: Evidence for δ18O buffering of the oceans by deep (> 5 km) seawater-hydrothermal circulation at mid-ocean ridges. *Journal of Geophysical Research*, *86*(B4), 2737–2755. https://doi.org/10.1029/JB086iB04p02737

Hamlyn, P. R., Keays, R. R., Cameron, W. E., Crawford, A. J., & Waldron, H. M. (1985). Precious metals in magnesian low-Ti lavas: Implications for metallogenesis and sulfur saturation in primary magmas. *Geochimica et Cosmochimica Acta*, *49*(8), 1797–1811. https://doi.org/10.1016/0016-7037(85)90150-4

Hickey-Vargas, R. (1998). Origin of the Indian Ocean-type isotopic signature in basalts from Philippine Sea plate spreading centers: An assessment of local versus large-scale processes. *Journal of Geophysical Research*, *103*(B9), 20963–20979. https://doi.org/10.1029/98JB02052

Hickey-Vargas, R. (2005). Basalt and tonalite from the Amami Plateau, northern West Philippine Basin: New Early Cretaceous ages and geochemical results, and their petrologic and tectonic implications. *Island Arc*, *14*(4), 653–665.

Holland, T. J. B., & Powell, R. (2003). Activity–composition relations for phases in petrological calculations: An asymmetric multicomponent formulation. *Contributions to Mineralogy and Petrology*, *145*, 492–501.

Holland, T. J. B., & Powell, R. (2011). An improved and extended internally consistent thermodynamic dataset for phases of petrological interest, involving a new equation of state for solids. *Journal of Metamorphic Geology*, *29*, 333–383.

Ishizuka, O., Kimura, J., Li, Y., Stern, R., Reagan, M., Taylor, R., et al. (2006). Early stages in the evolution of Izu–Bonin arc volcanism: New age, chemical, and isotopic constraints. *Earth and Planetary Science Letters*, *250*(1), 385–401. https://doi.org/10.1016/j.epsl.2006.08.007

Ishizuka, O., Tani, K., Reagan, M. K., Kanayama, K., Umino, S., Harigane, Y., et al. (2011). The timescales of subduction initiation and subsequent evolution of an oceanic island arc. *Earth and Planetary Science Letters*, *306*(3), 229–240. https://doi.org/10.1016/j.epsl.2011.04.006

Ishizuka, O., Taylor, R. N., Ohara, Y., & Yuasa, M. (2013). Upwelling, rifting, and age-progressive magmatism from the Oki-Daito mantle plume. *Geology*, *41*(9), 1011–1014. https://doi.org/10.1130/G34525.1

Ishizuka, O., Taylor, R. N., Umino, S., & Kanayama, K. (2020). Geochemical evolution of arc and slab following subduction initiation: A record from the Bonin islands, Japan. *Journal of Petrology*, *61*(5), 1–20. https://doi.org/10.1093/petrology/egaa050

Jenner, F. E., & O'Neill, H. S. C. (2012). Analysis of 60 elements in 616 ocean floor basaltic glasses. *Geochemistry, Geophysics, Geosystems*, *13*(2), Q02005. https://doi.org/10.1029/2011GC004009

Johnson, L. E., Fryer, P., Taylor, B., Silk, M., Jones, D. L., Sliter, W. V., et al. (1991). New evidence for crustal accretion in the outer Mariana fore arc: Cretaceous radiolarian cherts and mid-ocean ridge basalt-like lavas. *Geology*, *19*(8), 811–814.

Kamenetsky, V. S., Sobolev, A. V., Eggins, S. M., Crawford, A. J., & Arculus, R. J. (2002). Olivine-enriched melt inclusions in chromites from low-Ca boninites, Cape Vogel, Papua New Guinea: Evidence for ultramafic primary magma, refractory mantle source and enriched components. *Chemical Geology*, *183*(1–4), 287–303.

Kelley, K. A., Plank, T., Ludden, J., & Staudigel, H. (2003). Composition of altered oceanic crust at ODP Sites 801 and 1149. *Geochemistry, Geophysics, Geosystems*, *4*(6), 8910. https://doi.org/10.1029/2002GC000435

Kempton, P. D., Hawkesworth, C. J., & Fowler, M. (1991). Geochemistry and isotopic composition of gabbros from layer 3 of the Indian Ocean crust, Hole 735B. In R. P. Von Herzen & P. T. Robinson (Eds.), *Proceedings of the ocean drilling program scientific results* (Vol. 118, pp. 127–143). College Station, TX: Ocean Drilling Program.

Kendrick, M. A., Arculus, R., Burnard, P., & Honda, M. (2013). Quantifying brine assimilation by submarine magmas: Examples from the Galápagos Spreading Centre and Lau Basin. *Geochimica et Cosmochimica Acta*, *123*, 150–165. https://doi.org/10.1016/j.gca.2013.09.012

Kendrick, M. A., Hémond, C., Kamenetsky, V. S., Danyushevsky, L., Devey, C. W., Rodemann, T., et al. (2017). Seawater cycled throughout Earth's mantle in partially serpentinized lithosphere. *Nature Geoscience*, *10*(3), 222–228. https://doi.org/10.1038/NGEO2902

Kent, A. J., Peate, D. W., Newman, S., Stolper, E. M., & Pearce, J. A. (2002). Chlorine in submarine glasses from the Lau Basin: Seawater contamination and constraints on the composition of slab-derived fluids. *Earth and Planetary Science Letters*, *202*(2), 361–377.

Klein, E. M., & Langmuir, C. H. (1987). Global correlations of ocean ridge basalt chemistry with axial depth and crustal thickness. *Journal of Geophysical Research*, *92*(B8), 8089–8115. https://doi.org/10.1029/JB092iB08p08089

Kuroda, N., & Shiraki, K. (1975). Boninite and related rocks of Chichijima, Bonin islands, Japan. *Reports of Faculty of Science Shizuoka University*, *10*, 145–155.

Kyser, T. K., & O'Neil, J. R. (1984). Hydrogen isotope systematics of submarine basalts. *Geochimica et Cosmochimica Acta*, *48*(10), 2123–2133.

Langmuir, C. H., Bezos, A., Escrig, S., & Parman, S. W. (2006). Chemical systematics and hydrous melting of the mantle in back-arc basins. *Geophysical Monograph-American Geophysical Union*, *166*, 87–146. https://doi.org/10.1029/166GM07

le Roux, P. J., Shirey, S. B., Hauri, E. H., Perfit, M. R., & Bender, J. F. (2006). The effects of variable sources, processes and contaminants on the composition of northern EPR MORB (8–10 N and 12–14 N): Evidence from volatiles (H_2O, CO_2, S) and halogens (F, Cl). *Earth and Planetary Science Letters*, *251*(3–4), 209–231. https://doi.org/10.1016/j.epsl.2006.09.012

Li, H. Y., Taylor, R., Prytulak, J., Shervais, J., Ryan, J. G., Godard, M., et al. (2019). Radiogenic isotopes document the start of subduction in the Western Pacific. *Earth and Planetary Science Letters*, *518*, 197–210. https://doi.org/10.1016/j.epsl.2019.04.041

Li, Y. B., Kimura, J.-I., Machida, S., Ishii, T., Ishiwatari, A., Maruyama, S., et al. (2013). High-Mg adakite and low-Ca boninite from a Bonin Fore-arc seamount: Implications for the reaction between slab melts and depleted mantle. *Journal of Petrology*, *54*(6), 1149–1175. https://doi.org/10.1093/petrology/egt008

Lissenberg, C. J., MacLeod, C. J., & Bennett, E. N. (2019). Consequences of a crystal mush-dominated magma plumbing system: A mid-ocean ridge perspective. *Philosophical Transactions of the Royal Society A*, *377*(2139), 20180014. https://doi.org/10.1098/rsta.2018.0014

Loewen, M. W., Graham, D., Bindeman, I. N., & Garcia, M. O. (2019). Hydrogen isotopes in high $^3He/^4He$ submarine basalts: Primordial vs. recycled water and the veil of mantle enrichment. *Earth and Planetary Science Letters*, *508*, 62–73. https://doi.org/10.1016/j.epsl.2018.12.012

Martin, E., Bindeman, I. N., Balan, E., Palandri, J., Seligman, A., & Villemant, B. (2017). Hydrogen isotope determination by TC/EA technique in application to volcanic glass as a window into secondary hydration. *Journal of Volcanology and Geothermal Research*, *348*, 49–61. https://doi.org/10.1016/j.jvolgeores.2017.10.013

Mathez, E. A. (1976). Sulfur solubility and magmatic sulphides in submarine basalt glass. *Journal of Geophysical Research*, *81*(23), 4269–4276. https://doi.org/10.1029/JB081i023p04269

Maunder, B., Prytulak, J., Goes, S., & Reagan, M. (2020). Rapid subduction initiation and magmatism in the Western Pacific driven by internal vertical forces. *Nature Communications*, *11*, 1874. https://doi.org/10.1038/s41467-020-15737-4

Michael, P. J., & Schilling, J. G. (1989). Chlorine in mid-ocean ridge magmas: Evidence for assimilation of seawater-influenced components. *Geochimica et Cosmochimica Acta*, *53*(12), 3131–3143. https://doi.org/10.1029/98JB00791

Miyashiro, A. (1974). Volcanic rock series in island arcs and active continental margins. *American Journal of Science*, *274*, 321–355.

Pagé, P., Bédard, J. H., & Tremblay, A. (2009). Geochemical variations in a depleted fore-arc mantle: The Ordovician Thetford Mines Ophiolite. *Lithos*, *113*(1–2), 21–47. https://doi.org/10.1016/j.lithos.2009.03.030

Paton, C., Hellstrom, J., Paul, B., Woodhead, J., & Hergt, J. (2011). Iolite: Freeware for the visualisation and processing of mass spectrometric data. *Journal of Analytical Atomic Spectrometry*, *26*(12), 2508–2518. https://doi.org/10.1039/C1JA10172B

Pearce, J. A., Kempton, P. D., Nowell, G. M., & Noble, S. R. (1999). Hf-Nd element and isotope perspective on the nature and provenance of mantle and subduction components in Western Pacific arc-basin systems. *Journal of Petrology*, *40*(11), 1579–1611.

Pearce, J. A., & Reagan, M. K. (2019). Identification classification and interpretation of boninites from the Recent-Eoarchean geologic record using Si-Mg-Ti systematics. *Geosphere*, *15*, 1–30. https://doi.org/10.1130/GES01661.1

Pearce, J. A., & Robinson, P. T. (2010). The Troodos ophiolitic complex probably formed in a subduction initiation, slab edge setting. *Gondwana Research*, *18*(1), 60–81. https://doi.org/10.1016/j.gr.2009.12.003

Pearce, J. A., van der Laan, S. R., Arculus, R. J., Murton, B. J., Ishii, T., Peate, D. W., et al. (1992). Boninite and harzburgite from Leg 125 (Bonin-Mariana forearc): A case study of magma genesis during the initial stages of subduction. In P. Fryer, J. A. Pearce & L. B. Stokking (Eds.), *Proceedings of the ocean drilling program, scientific results* (Vol. 125, pp. 623–659). College Station, TX: Ocean Drilling Program.

Plank, T., & Langmuir, C. H. (1998). The chemical composition of subducting sediment and its consequences for the crust and mantle. *Chemical Geology*, *145*, 325–394.

Powell, R., & Holland, T. J. B. (1988). An internally consistent dataset with uncertainties and correlations: 3. Applications to geobarometry, worked examples and a computer program. *Journal of Metamorphic Geology*, *6*, 173–204.

Prowatke, S., & Klemme, S. (2006). Trace element partitioning between apatite and silicate melts. *Geochimica et Cosmochimica Acta*, *70*(17), 4513–4527. https://doi.org/10.1016/j.gca.2006.06.162

Qi, H., Coplen, T. B., Gehre, M., Vennemann, T. W., Brandt, W. A., Geilmann, H., et al. (2017). New biotite and muscovite isotopic reference materials, USGS57 and USGS58, for d2H measurements-a replacement for NBS 30. *Chemical Geology*, *467*, 89–99. https://doi.org/10.1016/j.chemgeo.2017.07.027

Reagan, M. K., Hanan, B. B., Heizler, M. T., Hartman, B. S., & Hickey-Vargas, R. (2008). Petrogenesis of volcanic rocks from Saipan and Rota, Mariana Islands, and implications for the evolution of nascent island arcs. *Journal of Petrology*, *49*(3), 441–464. https://doi.org/10.1093/petrology/egm087

Reagan, M. K., Heaton, D. E., Schmitz, M. D., Pearce, J. A., Shervais, J. W., & Koppers, A. A. (2019). Forearc ages reveal extensive short-lived and rapid seafloor spreading following subduction initiation. *Earth and Planetary Science Letters*, *506*, 520–529. https://doi.org/10.1016/j.epsl.2018.11.020

Reagan, M. K., Ishizuka, O., Stern, R. J., Kelley, K. A., Ohara, Y., Blichert-Toft, J., et al. (2010). Fore-arc basalts and subduction initiation in the Izu-Bonin-Mariana system. *Geochemistry, Geophysics, Geosystems*, *11*(3), Q03X12. https://doi.org/10.1029/2009GC002871

Reagan, M. K., McClellandGirard, W. C. G., Goff, K. R., Peate, D. W., Ohara, Y., & Stern, R. J. (2013). The geology of the southern Mariana fore-arc crust: Implications for the scale of Eocene volcanism in the western Pacific. *Earth and Planetary Science Letters*, *380*, 41–51. http://dx.doi.org/10.1016/j.epsl.2013.08.013

Reagan, M. K., Pearce, J. A., Petronotis, K., Almeev, R. R., Avery, A. J., Carvallo, C., et al. (2017). Subduction initiation and ophiolite crust: New insights from IODP drilling. *International Geology Review*, *59*(11), 1–12. https://doi.org/10.1080/00206814.2016.1276482

Reagan, M. K., Pearce, J. A., Petronotis, K., & The Expedition 352 Scientists. (2015). Izu-Bonin-Mariana fore arc. In M. K. Reagan, J. A. Pearce, K. Petronotis, & The Expedition 352 Scientists (Eds.), *Proceedings of the International Ocean Discovery Program* (Vol. 352). College Station, TX: International Ocean Discovery Program. https://doi.org/10.14379/iodp.proc.352.101.2015

Rehkämper, M., & Hofmann, A. W. (1997). Recycled ocean crust and sediment in Indian Ocean MORB. *Earth and Planetary Science Letters*, *147*(1–4), 93–106. https://doi.org/10.1016/S0012-821X(97)00009-5

Resing, J. A., Rubin, K. H., Embley, R. W., Lupton, J. E., Baker, E. T., Dziak, R. P., et al. (2011). Active submarine eruption of boninite in the northeastern Lau Basin. *Nature Geoscience*, *4*(11), 799. https://doi.org/10.1038/ngeo1275

Ryan, W. B. F., Carbotte, S. M., Coplan, J., O'Hara, S., Melkonian, A., Arko, R., et al. (2009). Global Multi-Resolution Topography (GMRT) synthesis data set. *Geochemistry Geophysics Geosystems*, *10*, Q03014. https://doi.org/10.1029/2008GC002332

Ryan, J. G., & Langmuir, C. H. (1987). The systematics of lithium abundances in young volcanic rocks. *Geochimica et Cosmochimica Acta*, *51*(6), 1727–1741. https://doi.org/10.1016/0016-7037(87)90351-6

Ryan, J. G., Shervais, J. W., Li, Y., Reagan, M. K., Li, H., Heaton, D., et al. (2017). Application of a handheld X-ray fluorescence spectrometer for real-time, high-density quantitative analysis of drilled igneous rocks and sediments during IODP Expedition 352. *Chemical Geology*, *451*, 55–66. https://doi.org/10.1016/j.chemgeo.2017.01.007

Sano, T., Miyoshi, M., Ingle, S., Banerjee, N. R., Ishimoto, M., & Fukuoka, T. (2008). Boron and chlorine contents of upper oceanic crust: Basement samples from IODP hole 1256D. *Geochemistry, Geophysics, Geosystems*, *9*(12), Q12O15. https://doi.org/10.1029/2008GC002182

Schmidt, M. W., & Jagoutz, O. (2017). The global systematics of primitive arc melts. *Geochemistry, Geophysics, Geosystems*, *18*, 2817–2854. https://doi.org/10.1002/2016GC006699

Shaw, A. M., Hauri, E. H., Behn, M. D., Hilton, D. R., Macpherson, C. G., & Sinton, J. M. (2012). Long-term preservation of slab signatures in the mantle inferred from hydrogen isotopes. *Nature Geoscience*, *5*(3), 224–228. https://doi.org/10.1038/NGEO1406

Shervais, J. W. (1982). Ti-V plots and the petrogenesis of modern and ophiolitic lavas. *Earth and Planetary Science Letters*, *59*(1), 101–118.

Shervais, J. W. (2001). Birth, death, and resurrection: The life cycle of suprasubduction zone ophiolites. *Geochemistry, Geophysics, Geosystems*, *2*, 2000GC000080. https://doi.org/10.1029/2000GC000080

Shervais, J. W., & Jean, M. M. (2012). Inside the subduction factory: Modeling fluid mobile element enrichment in the mantle wedge above a subduction zone. *Geochimica et Cosmochimica Acta*, *95*, 270–285. https://doi.org/10.1016/j.gca.2012.07.006

Shervais, J. W., Reagan, M. K., Godard, M., J. A., Prytulak, J., Ryan, J. G., Pearce, J. A., et al. (2020). Magmatic response to subduction initiation, Part II: Boninites and related rocks of the Izu-Bonin Arc from IOPD Expedition 352. *Geochemistry, Geophysics, Geosystems*, *21*, e2020GC009093. https://doi.org/10.1029/2020GC009093

Shervais, J. W., Reagan, M. K., Haugen, E., Almeev, R., Whattam, S. A., Pearce, J. A., et al. (2019). Magmatic response to subduction initiation, part I: Fore-arc basalts of the Izu-Bonin Arc from IODP Expedition 352. *Geochemistry, Geophysics, Geosystems*, *20*, 314–338. https://doi.org/10.1029/2018GC007731

Shimizu, K., Ito, M., Chang, Q., Miyazaki, T., Ueki, K., Toyama, C., et al. (2019). Identifying volatile mantle trend with the water–fluorine–cerium systematics of basaltic glass. *Chemical Geology*, *522*, 283–294. https://doi.org/10.1016/j.chemgeo.2019.06.014

Shimizu, K., Ushikubo, T., Hamada, M., Itoh, S., Higashi, Y., Takahashi, E., et al. (2017). H_2O, CO_2, F, S, Cl, and P_2O_5 analyses of silicate glasses using SIMS: Report of volatile standard glasses. *Geochemical Journal*, *51*(4), 299–313. https://doi.org/10.2343/geochemj.2.0470

Stakes, D. S., & Taylor, H. P., Jr. (1992). The northern Samail ophiolite: An oxygen isotope, microprobe, and field study. *Journal of Geophysical Research*, *97*(B5), 7043–7080. https://doi.org/10.1029/91JB02743

Stern, R. J., & Bloomer, S. H. (1992). Subduction zone infancy: Examples from the Eocene Izu-Bonin-Mariana and Jurassic California arcs. *The Geological Society of America Bulletin*, *104*(12), 1621–1636.

Taylor, B., & Huchon, P. (2002). Active continental extension in the western Woodlark Basin: a synthesis of Leg 180 results. In Huchon, P., Taylor, B., and Klaus, A. (Eds.), Proc. ODP, Sci. Results, 18 0: College Station, TX (Ocean Drilling Program), 1–36. https://doi.org/10.2973/odp.proc.sr.180.150.2002

Taylor, B., & Goodliffe, A. M. (2004). The West Philippine Basin and the initiation of subduction, revisited. *Geophysical Research Letters*, *31*(12), L12602. https://doi.org/10.1029/2004GL020136

Taylor, H. P., Jr., & Sheppard, S. M. F. (1986). Igneous rocks, m. Processes of isotopic fractionation and isotope systematics. In J. W. Valley, H. P. Taylor Jr. & J. R. O'Neil (Eds.) *Stable isotopes in high temperature processes* (Reviews in mineralogy, 16) (Vol. 227, pp. 227–272). Washington, DC: Mineralogical Society of America.

Taylor, R. N., Nesbitt, R. W., Vidal, P., Harmon, R. S., Auvray, B., & Croudace, I. W. (1994). Mineralogy, chemistry, and genesis of the boninite series volcanics, Chichijima, Bonin Islands, Japan. *Journal of Petrology*, *35*(3), 577–617. https://doi.org/10.1093/petrology/35.3.577

Tiepolo, M., Oberti, R., & Vannucci, R. (2002). Trace-element incorporation in titanite: Constraints from experimentally determined solid/liquid partition coefficients. *Chemical Geology*, *191*(1–3), 105–119. https://doi.org/10.1016/S0009-2541(02)00151-1

Umino, S., Kitamura, K., Kanayama, K., Tamura, A., Sakamoto, N., Ishizuka, O., et al. (2015). Thermal and chemical evolution of the subarc mantle revealed by spinel-hosted melt inclusions in boninite from the Ogasawara (Bonin) Archipelago, Japan. *Geology*, *43*(2), 151–154. https://doi.org/10.1130/G36191.1

Valetich, M. J., Mavrogenes, J., Arculus, R., & Umino, S. (2019). Evolution of chalcophile elements in the magmas of the Bonin Islands. *Chemical Geology*, *508*, 234–249. https://doi.org/10.1016/j.chemgeo.2018.07.011

Wanless, V. D., Perfit, M. R., Ridley, W. I., Wallace, P. J., Grimes, C. B., & Klein, E. M. (2011). Volatile abundances and oxygen isotopes in basaltic to dacitic lavas on mid-ocean ridges: The role of assimilation at spreading centers. *Chemical Geology*, *287*(1–2), 54–65. https://doi.org/10.1016/j.chemgeo.2011.05.017

Warren, J. M., & Hauri, E. H. (2014). Pyroxenes as tracers of mantle water variations. *Journal of Geophysical Research: Solid Earth*, *119*, 1851–1881. https://doi.org/10.1002/2013JB010328

Whattam, S. A., Shervais, J. W., Reagan, M. K., Coulthard, D. A., Jr., Pearce, J. A., Jones, P., et al. (2020). Mineral compositions and thermobarometry of basalts and boninites recovered during IODP Expedition 352 to the Bonin forearc. *American Mineralogist*, *105*, 1490–1507. https://doi.org/10.2138/am-2018-6640

White, R. W., Powell, R., Holland, T. J. B., Johnson, T. E., & Green, E. C. R. (2014). New mineral activity–composition relations for thermodynamic calculations in metapelitic systems. *Journal of Metamorphic Geology*, *32*, 261–286.

White, R. W., Powell, R., Holland, T. J. B., & Worley, B. A. (2000). The effect of TiO_2 and Fe_2O_3 on metapelitic assemblages at greenschist and amphibolite facies conditions: Mineral equilibria calculations in the system K_2O–FeO–MgO–Al_2O_3–SiO_2–H_2O–TiO_2–Fe_2O_3. *Journal of Metamorphic Geology*, *18*, 497–511.

Woelki, D., Regelous, M., Haase, K. M., Romer, R. H., & Beier, C. (2018). Petrogenesis of boninitic lavas from the Troodos Ophiolite, and comparison with Izu–Bonin–Mariana fore-arc crust. *Earth and Planetary Science Letters*, *498*, 203–214. https://doi.org/10.1016/j.epsl.2018.06.041

Yogodzinski, G. M., Bizimis, M., Hickey-Vargas, R., McCarthy, A., Hocking, B. D., Savov, I. P., et al. (2018). Implications of Eocene-age Philippine Sea and forearc basalts for initiation and early history of the Izu-Bonin-Mariana arc. *Geochimica et Cosmochimica Acta*, *228*, 136–156. https://doi.org/10.1016/j.gca.2018.02.047

Yuan, C., Sun, M., Zhou, M. F., Xiao, W., & Zhou, H. (2005). Geochemistry and petrogenesis of the Yishak volcanic sequence, Kudi ophiolite, West Kunlun (NW China): Implications for the magmatic evolution in a subduction zone environment. *Contributions to Mineralogy and Petrology*, *150*(2), 195–211. https://doi.org/10.1007/s00410-005-0012-0

Zhang, C., Wang, L. X., Marks, M. A., France, L., & Koepke, J. (2017). Volatiles (CO_2, S, F, Cl, Br) in the dike-gabbro transition zone at IODP Hole 1256D: Magmatic imprint versus hydrothermal influence at fast-spreading mid-ocean ridge. *Chemical Geology*, *459*, 43–60. https://doi.org/10.1016/j.chemgeo.2017.04.002

References From Supporting Information

Paton, C., Hellstrom, J., Paul, B., Woodhead, J., & Hergt, J. (2011). Iolite: Freeware for the visualisation and processing of mass spectrometric data. *Journal of Analytical Atomic Spectrometry*, *26*(12), 2508–2518. https://doi.org/10.1039/C1JA10172B

Qi, H., Coplen, T. B., Gehre, M., Vennemann, T. W., Brandt, W. A., Geilmann, H., et al. (2017). New biotite and muscovite isotopic reference materials, USGS57 and USGS58, for d2H measurements–a replacement for NBS 30. *Chemical Geology*, *467*, 89–99. https://doi.org/10.1016/j.chemgeo.2017.07.027